This title page provides information to assist publication of this work.

Title: A divergence-free high-order Spectral Difference method with Constrained Transport (SDCT) for ideal compressible magnetohydrodynamics

Authors: Kuangxu Chen*, Chunlei Liang (Department of Mechanical and Aerospace Engineering, Clarkson University, Potsdam, USA). * is the corresponding author.

Contact information for Kuangxu Chen: kuchen@clarkson.edu (email), 3152686586 (Phone Number and Fax), ORCID: 0000-0002-1627-1177

Contact information for Chunlei Liang: cliang@clarkson.edu (email), 3152686575 (Phone Number and Fax), ORCID: 0000-0002-8646-0707

A divergence-free high-order Spectral Difference method with Constrained Transport (SDCT) for ideal compressible magnetohydrodynamics

Kuangxu Chen, Chunlei Liang

Clarkson University

Abstract

When the high-order discontinuous Galerkin or Spectral Difference (SD) method is used to discretize ideal magnetohydrodynamic (MHD) equations, it is challenging to satisfy the divergence-free constraint $\nabla \cdot \mathbf{B} = 0$ for the magnetic field over long time integration. To ensure that the discrete $\nabla \cdot \mathbf{B}$ equals to zero exactly and globally, the SD method is integrated with an unstaggered Constrained Transport approach (SDCT) by replacing the magnetic field with the curl of the magnetic potential at every time step. The SDCT method stores the variables for the hydrodynamics and the magnetic field at the same set of solution points, which avoids designing 2D Riemann solvers and preserves the compactness of the stencil for spatial discretization. Moreover, the additional computational cost is less than 1/8 of that without the constrained transport. Meanwhile, artificial dissipation terms can be added to perform sharp shock capturing. The SDCT method is found to maintain the divergence error of the magnetic field at the level of machine round-off error throughout simulations and have excellent convergence in test cases with and without shocks.

Keywords: Magnetohydrodynamics, Spectral, High-Order, Constrained Transport

1. INTRODUCTION

One implication of the MHD equations is that the divergence-free constraint of the magnetic field should be maintained forever if the initial magnetic field is divergence-free. However, in numerical computation of the MHD equations, the discrete divergence of the magnetic field is not exactly zero. The $\nabla \cdot \mathbf{B}$ error stemming from the spatial discretization error may increase with time integration. The accumulation effect of this error would induce unphysical behaviors of the MHD system, leading to decreased stability and accuracy of numerical methods [1, 2, 3]. Therefore, how to control the $\nabla \cdot \mathbf{B}$ error over long-period time integration is a major challenge for simulations of MHD processes.

There are two approaches to treat the $\nabla \cdot \mathbf{B}$ error. The first approach is the divergence cleaning, in which the divergence error is viewed as non-zero and is transported to the domain boundaries in a behavior similar to propagating waves of hyperbolic equations [4]. The second approach is based on the divergence-free reconstruction to achieve $\nabla \cdot \mathbf{B} = 0$ in the discrete sense exactly by design. Evans and Hawley [5] proposed a Constrained Transport (CT) method based on a staggered representation of the magnetic field to preserve $\nabla \cdot \mathbf{B} = 0$ exactly on the discretized level. This kind of CT method of staggered fashion was popular and has numerous variants, which are extended to high-order version [6] and adapted to adaptive mesh refinement (AMR) [7]. But putting solutions of the Euler sub-system describing the flow field and solutions of the magnetic field at different locations undoubtedly adds unnecessary complexity to the MHD solvers. Then Tóth [3] showed that a staggered magnetic field is not necessary, and proposed an unstaggered CT method by solving the magnetic potential \mathbf{A} instead of the

Email address: kuchen@clarkson.edu cliang@clarkson.edu (Kuangxu Chen, Chunlei Liang)

magnetic field $\mathbf{B} = \nabla \times \mathbf{A}$. Rossmanith [8] developed a general unstaggered CT framework by adding one additional equation describing the evolution of the magnetic potential and using the discrete curl of the magnetic potential to correct the predicted magnetic field. This framework was later extended to adapt to high-order numerical schemes, e.g., finite difference weighted Essentially Non-Oscillatory (ENO) schemes [9] and targeted ENO schemes [10]. The current study is built upon this framework to ensure exact divergence-free reconstruction of the magnetic field.

Apart from taking care of the $\nabla \cdot \mathbf{B}$ error, developing high-order accurate methods with sharp shock capturing capability and excellent scalability on parallel computers is another goal of the current study. In this paper, the Spectral Difference (SD) method [11, 12, 13, 14], a newly developed efficient high-order approach of discontinuous type, is employed to achieve this goal. The SD method is efficient since operations are completed in a one-dimensional fashion, and the equations are solved in differential form, removing explicit surface and volume integral integrations [15]. Additionally, solution and flux reconstructions are completed locally per cell, increasing the parallelization of the implementation. These properties of the SD method offer a promising route to run large-scale simulations of hitherto intractable astrophysical MHD flows on modern parallel computers with unprecedented efficiency. To keep these advantages, an artificial dissipation method which keeps the compactness of the stencil of the SD method is employed to perform shock capturing. For producing oscillation-free solutions, additional dissipation is added to unsmooth region detected by the discontinuity sensor. With reduction of the mesh size, the artificial dissipation will decrease correspondingly, and the numerical solution will converge.

Up to now, the SD method has contributed to the astrophysical community in terms of hydrodynamic simulation due to its spectral accuracy, great flexibility and suitability for highperformance computing. A massively parallel Compressible High-ORder Unstructured Spectral difference (CHORUS) code was developed by Wang, Liang and Miesch [16] for simulating stratified convection in rotating spherical shells. This code was later applied to performing global 3D simulations of thermal convection in oblate solar-type stars [17]. But the CHORUS code only includes hydrodynamic simulation part. In our previous efforts, the MHD version of the CHORUS code based on a Generalised Lagrange Multiplier (GLM) divergence cleaning approach were built [18, 19]. However, when it was applied to solar convection simulation which spans a long time period, the accumulation of the $\nabla \cdot \mathbf{B}$ error gradually drove the solution to blow up [20]. Moreover, in the GLM-MHD formulation, ad hoc parameters are difficult to adjust. A novel high-order SD method for the induction equation proposed by Veiga in [21] might be useful for avoiding these problems. This new SD method is a high-order extension of the original CT method built on the staggered grids. It distributes solution points of B_x , B_y and B_z in a staggered fashion, which is different from traditional SD method. Due to this special distribution, one major difficulty to extend it to the ideal MHD equations is to solve 2D Riemann problems at nodal points or element edges. But designing an accurate and robust 2D Riemann solver in the context of ideal MHD can be challenging. The current study hopes to avoid designing 2D Riemann solvers but still preserve advantages of the CT method, e.g., involving no problem-dependent tuning parameters and preserving the discrete $\nabla \cdot \mathbf{B}$ to the accuracy of machine round-off error. The proposed method should be stable and accurate for long time integration. Thus it can offer great flexibility and robustness for predicting challenging MHD flows from the astrophysical background, e.g., three-dimensional solar flares.

The current study is novel in successfully combining the high-order Spectral Difference (SD) method and the Constrained Transport (CT) approach to solve the ideal compressible MHD equations. The proposed new method is named as SDCT method.

2. GOVERNING EQUATIONS

The dynamics of electrically conducting fluid flow are often modeled by MHD equations. The conservative form of the ideal MHD equations can be written as

$$\frac{\partial}{\partial t} \begin{pmatrix} \rho \mathbf{U} \\ \rho \mathbf{U} \\ e \\ \mathbf{B} \end{pmatrix} + \nabla \cdot \begin{pmatrix} \rho \mathbf{U} \otimes \mathbf{U} + (p + \frac{1}{2} \|\mathbf{B}\|^2) \mathcal{I} - \mathbf{B} \otimes \mathbf{B} \\ \mathbf{U}(e + p + \frac{1}{2} \|\mathbf{B}\|^2) - \mathbf{B}(\mathbf{U} \cdot \mathbf{B}) \\ \mathbf{U} \otimes \mathbf{B} - \mathbf{B} \otimes \mathbf{U} \end{pmatrix} = \mathbf{0}, \tag{1}$$

where ρ , p and e are the density, pressure and total energy respectively, $\|\cdot\|$ is the Euclidean vector norm, $\mathbf{U} = (u, v, w)^T$ is the velocity vector, and $\mathbf{B} = (B_x, B_y, B_z)^T$ is the magnetic field. The total energy e is defined as

$$e = \frac{p}{\gamma - 1} + \frac{1}{2}\rho \|\mathbf{U}\|^2 + \frac{1}{2} \|\mathbf{B}\|^2,$$
 (2)

where γ is the specific ratio of ideal gas.

In two-dimensional domain, the governing equations for viscous MHD flow is reduced to

$$\frac{\partial \mathbf{Q}}{\partial t} + \frac{\partial \mathbf{F}}{\partial x} + \frac{\partial \mathbf{G}}{\partial y} = \mathbf{0},\tag{3}$$

where $\mathbf{Q} = (\rho, \rho u, \rho v, \rho w, e, B_x, B_y, B_z)^T$ is the vector of conserved variables. \mathbf{F} and \mathbf{G} are the fluxes, which are composed of the inviscid and viscous parts,

$$\mathbf{F} = \mathbf{F}_{inv} - \mathbf{F}_{vis},$$

$$\mathbf{G} = \mathbf{G}_{inv} - \mathbf{G}_{vis}.$$
(4)

The inviscid fluxes are

$$\mathbf{F}_{inv} = \begin{pmatrix} \rho u \\ \rho u^{2} + p + \frac{1}{2} \|\mathbf{B}\|^{2} - B_{x}^{2} \\ \rho uv - B_{x}B_{y} \\ \rho uw - B_{x}B_{z} \\ (e + p + \frac{1}{2} \|\mathbf{B}\|^{2})u - (uB_{x} + vB_{y})B_{x} \\ 0 \\ uB_{y} - vB_{x} \\ uB_{z} - wB_{x} \end{pmatrix}$$
(5)

$$\mathbf{G}_{inv} = \begin{pmatrix} \rho v \\ \rho uv - B_x B_y \\ \rho v^2 + p + \frac{1}{2} \|\mathbf{B}\|^2 - B_y^2 \\ \rho vw - B_y B_z \\ (e + p + \frac{1}{2} \|\mathbf{B}\|^2) v - (uB_x + vB_y) B_y \\ -(uB_y - vB_x) \\ 0 \\ vB_z - wB_y \end{pmatrix},$$
(6)

The viscous fluxes are

$$\mathbf{F}_{vis} = \begin{pmatrix} 0 \\ \tau_{xx} \\ \tau_{yx} \\ \tau_{zx} \\ u\tau_{xx} + v\tau_{yx} + w\tau_{zx} \\ 0 \\ \eta J_{z} \\ \eta J_{y} \end{pmatrix}, \quad \mathbf{G}_{vis} = \begin{pmatrix} 0 \\ \tau_{xy} \\ \tau_{yy} \\ \tau_{zy} \\ u\tau_{xy} + v\tau_{yy} + w\tau_{zy} \\ -\eta J_{z} \\ 0 \\ \eta J_{x} \end{pmatrix},$$
 (7)

where

$$\mathbf{J} = \begin{cases} J_x = \frac{\partial B_z}{\partial y} - \frac{\partial B_y}{\partial z} \\ J_y = \frac{\partial B_x}{\partial z} - \frac{\partial B_z}{\partial x} \\ J_z = \frac{\partial B_y}{\partial x} - \frac{\partial B_x}{\partial y} \end{cases}$$
(8)

Here, η is the resistivity, τ_{ij} is the shear stress tensor which is related to velocity gradients as $\tau_{ij} = \mu(u_{i,j} + u_{j,i}) + \lambda \delta_{ij} u_{k,k}$, and μ is the dynamic viscosity, $\lambda = -2/3\mu$ based on Stokes' hypothesis, δ_{ij} is the Kronecker delta.

Note that the time evolutions of B_z and velocity in the z-direction are also computed, and all 8 conserved variables can be non-zero. But all variables depend only on (x, y) and t, and these 8 equations are solved on a 2D domain.

3. NUMERICAL METHODS

3.1. Spectral Difference (SD) Method

In this study, non-overlapping structured rectangular elements are employed to fill the computational domain. To facilitate construction of solution and flux polynomials, each rectangular element in the physical domain (x, y) is mapped to a standard square element in computational domain $(0 \le \xi \le 1, 0 \le \eta \le 1)$. The transformation can be written as

$$\begin{pmatrix} x \\ y \end{pmatrix} = \sum_{i=1}^{4} M_i(\xi, \eta) \begin{pmatrix} x_i \\ y_i \end{pmatrix},$$
 (9)

where $M_i(\xi, \eta)$ is the shape function at the *i*-th node,

$$M_i = \pm(\xi + \xi_i - 1)(\eta + \eta_i - 1), \quad i = 1, 2, 3, 4,$$
 (10)

 (ξ_i, η_i) and (x_i, y_i) are the coordinates of the *i*-th node in the computational and the physical domain respectively and the RHS of equation 10 takes '-' sign for i = 2, 4, and '+' otherwise. Suppose that all elements are rectangular, we have $x_1 = x_4$, $x_2 = x_3$, $y_1 = y_2$ and $y_3 = y_4$, and the Jacobian matrix for this transformation is

$$J = \frac{\partial(x,y)}{\partial(\xi,\eta)} = \begin{pmatrix} \Delta x & 0\\ 0 & \Delta y \end{pmatrix},\tag{11}$$

where Δx and Δy are the mesh size along two coordinate directions. After this transformation, the conservation law is expressed in the computational domain as

$$\frac{\partial \mathbf{Q}}{\partial t} + \frac{\partial \mathbf{F}}{\partial \xi} \frac{1}{\Delta x} + \frac{\partial \mathbf{G}}{\partial \eta} \frac{1}{\Delta y} = \mathbf{0}.$$
 (12)

In the standard computational element, two sets of points are defined, namely the solution points (SPs) and the flux points (FPs), as illustrated in Figure 1. In order to construct a degree (N-1) polynomial in each coordinate direction, N SPs in each direction are required. In each dimension, the SPs are chosen as the Chebyshev-Gauss points defined as

$$X_s = \frac{1}{2} [1 - \cos(\frac{2s - 1}{2N}\pi)], \quad s = 1, 2, \dots, N.$$
 (13)

The FPs (denoted by $X_{s+1/2}$) along each direction are chosen as: $X_{1/2}$ and $X_{N+1/2}$ on the boundaries plus (N-1) roots of the N-th order Legendre polynomial, as suggested by Huynh [22]. A n-th order Legendre polynomial can be determined by

$$P_n(\xi) = \frac{2n-1}{n} (2\xi - 1) P_{n-1}(\xi) - \frac{n-1}{n} P_{n-2}(\xi).$$
 (14)

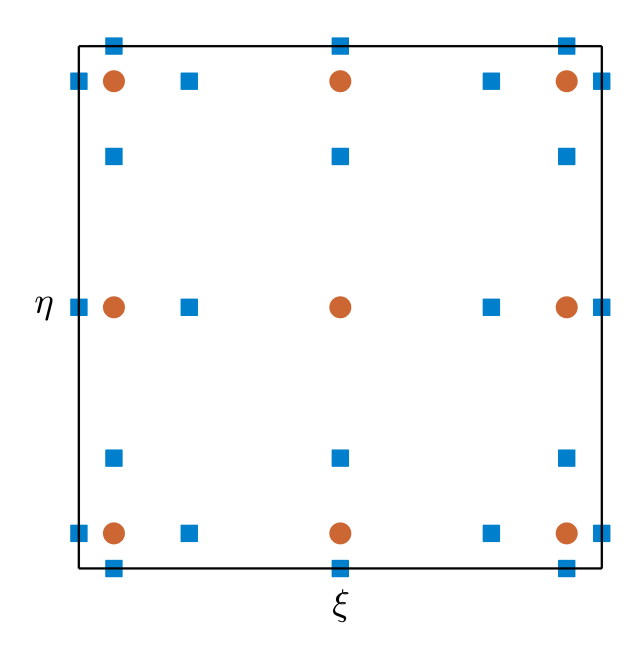


Figure 1: Distribution of solution points (circles) and flux points (squares) in the $\xi - \eta$ plane for a third-order SD scheme.

where the two starting polynomials are $P_{-1}(\xi) = 0$ and $P_0(\xi) = 1$. In the study of Liang et al. [23], this choice of FPs proved to be able to remove the weak instability [24] of choosing the Chebyshev-Gauss-Lobatto points as the FPs. Jameson [25] proved that for the one-dimensional linear advection, this choice ensures the stability of the SD method for all orders of accuracy.

The following Lagrange bases at the SPs and FPs are used to construct solution and flux polynomials,

$$h_i(X) = \prod_{s=1, s \neq i}^{N} \left(\frac{X - X_s}{X_i - X_s} \right), \tag{15}$$

$$l_{i+1/2}(X) = \prod_{s=0, s \neq i}^{N} \left(\frac{X - X_{s+1/2}}{X_{i+1/2} - X_{s+1/2}} \right).$$
 (16)

The reconstructed solution for the conserved variables is just the tensor products of the three one-dimensional Lagrange bases,

$$\mathbf{Q} = \sum_{j=1}^{N} \sum_{i=1}^{N} \mathbf{Q}_{i,j} \cdot h_i(\xi) \cdot h_j(\eta). \tag{17}$$

The conserved variables at the FPs are computed using equation 17. They are then used to compute the inviscid fluxes at the interior FPs. To ensure flux conservation, an approximate Riemann solver is needed to compute inviscid fluxes at element interfaces. The normal flux perpendicular to element interfaces is

$$\mathbf{F}_{n} = \begin{pmatrix} \rho V_{n} \\ \rho u V_{n} - B_{x} B_{n} + P_{t} n_{x} \\ \rho v V_{n} - B_{y} B_{n} + P_{t} n_{y} \\ \rho w V_{n} - B_{z} B_{n} + P_{t} n_{z} \\ V_{n} (e + P_{t}) - B_{n} (\mathbf{U} \cdot \mathbf{B}) \\ V_{n} B_{x} - B_{n} u \\ V_{n} B_{y} - B_{n} v \\ V_{n} B_{z} - B_{n} w \end{pmatrix},$$
(18)

where $P_t = p + \frac{1}{2} \|\mathbf{B}\|^2$ is the total pressure, $\mathbf{n} = (n_x, n_y, n_z)^T$ is the outward normal direction of element faces, subscript n represents projection in the normal direction,

$$V_n = \mathbf{U} \cdot \mathbf{n} = un_x + vn_y + wn_z$$

$$B_n = \mathbf{B} \cdot \mathbf{n} = B_x n_x + B_y n_y + B_z n_z.$$
(19)

The Local Lax-Friedrichs (LLF) numerical fluxes [26] are employed to compute common inviscid fluxes $\hat{\mathbf{F}}_n$ at the FPs located at the element interfaces,

$$\hat{\mathbf{F}}_n = \frac{1}{2} \left(\mathbf{F}_n^L + \mathbf{F}_n - \lambda_{\text{max}} (\mathbf{Q}^R - \mathbf{Q}^L) \right), \tag{20}$$

where superscripts 'L' and 'R' denote left and right states on interfaces. $\lambda_{\text{max}} = \mathbf{U} \cdot \mathbf{n} + c_f$ is the maximum absolute value of the characteristic speeds, and c_f is the speed of fast magnetosonic waves,

$$c_f = \left\{ \frac{1}{2} \left[a^2 + \frac{\|\mathbf{B}\|^2}{\rho} - \sqrt{\left(a^2 + \frac{\|\mathbf{B}\|^2}{\rho} \right)^2 - 4a^2 \frac{(\mathbf{B} \cdot \mathbf{n})^2}{\rho}} \right] \right\}.$$
 (21)

The speed of sound $a = \sqrt{\gamma p/\rho}$. For more information, [27] provided a detailed analysis on the eigensystem of ideal MHD equations. After the fluxes are obtained at all FPs, flux polynomials for computational elements are reconstructed as

$$\mathbf{F} = \sum_{j=1}^{N} \sum_{i=0}^{N} \mathbf{F}_{i+1/2,j} \cdot l_{i+1/2}(\xi) \cdot h_{j}(\eta),$$

$$\mathbf{G} = \sum_{j=0}^{N} \sum_{i=1}^{N} \mathbf{G}_{i,j+1/2} \cdot h_{i}(\xi) \cdot l_{j+1/2}(\eta).$$
(22)

Then differentiation of the flux polynomials gives the spatial derivatives of the fluxes at all SPs, i.e.,

$$\left[\frac{\partial \mathbf{F}}{\partial \xi}\right]_{i,j} = \sum_{r=0}^{N} \mathbf{F}_{r+1/2,j} \cdot l'_{r+1/2}(X_i),$$

$$\left[\frac{\partial \mathbf{G}}{\partial \eta}\right]_{i,j} = \sum_{r=0}^{N} \mathbf{G}_{i,r+1/2} \cdot l'_{r+1/2}(X_j).$$
(23)

To guarantee continuity of the solution, the common solution at the interfaces is computed as the average of solutions from the left and right elements, (also known as the BR1 scheme [28])

$$\mathbf{Q}^{\text{com}} = \frac{1}{2} (\mathbf{Q}^L + \mathbf{Q}^R). \tag{24}$$

Then we need to compute solution gradients $\nabla \mathbf{Q}$ in preparation for computation of the viscous fluxes. Sun et al. [29] proposed an expression to efficiently compute solution gradients in the physical domain for arbitrary unstructured mesh while that expression reduces to

$$\left[\frac{\partial \mathbf{Q}}{\partial x}\right]_{j} = \frac{\partial \mathbf{Q}}{\partial \xi} \frac{1}{\Delta x} = \sum_{r=0}^{N} \mathbf{Q}_{r+1/2,j} \cdot l'_{r+1/2}(\xi),
\left[\frac{\partial \mathbf{Q}}{\partial y}\right]_{i} = \frac{\partial \mathbf{Q}}{\partial \eta} \frac{1}{\Delta y} = \sum_{r=0}^{N} \mathbf{Q}_{i,r+1/2} \cdot l'_{r+1/2}(\eta).$$
(25)

Then solution gradients are extrapolated from the SPs to the FPs in the same way solutions do. Then common gradients on the interfaces are computed by averaging. After getting both

solutions and solution gradients at the FPs, viscous fluxes at the FPs are computed by using equation 7. Evaluation of the gradients of the viscous fluxes follows the same way as in the inviscid fluxes.

Once the derivatives of all fluxes are computed at all SPs, the governing equations can be written in a residual form as

$$\left[\frac{\partial \mathbf{Q}}{\partial t}\right]_{i,j} = -\left[\frac{\partial F}{\partial \xi} \frac{1}{\Delta x} + \frac{\partial G}{\partial \eta} \frac{1}{\Delta y}\right]_{i,j} = \mathcal{R}_{i,j},\tag{26}$$

where $\mathcal{R}_{i,j}$ is the residual at the (i,j)-th SP. For time marching, we employ an explicit third-order strong-stability-preserving five-stage Runge-Kutta scheme [30].

3.2. Artificial Dissipation for Shock Capturing

Artificial viscosity μ_{Δ} is added for suppressing spurious oscillations near the shock interfaces. Persson and Peraire proposed a simple and suitable smoothness sensor for high-order numerical methods in [31]. That sensor can detect the discontinuities of the solutions in the interiors of elements in a robust way. Based on the smoothness sensor, a Laplacian or physical artificial viscosity is formulated to act as additional dissipation near the discontinuities. Lodato et al. [32] extended this method to the SD scheme and applied it to the Direct Numerical Simulation of supersonic flows with complex shock interaction. In this study, the smoothness sensor follows the formulation in [31, 32], and the physical artificial viscosity is employed.

The idea of computation of the smoothness sensor is to measure the difference between the original solutions and the solutions which have been smoothed to a low-order level. To smooth the solutions, restriction and prolongation are needed. Restriction means interpolation of the solutions from the SPs of the N-th order scheme to SPs of the (N-1)-th order, i.e.,

$$\hat{Q}_{\alpha,\beta} = \sum_{j=1}^{N} \sum_{i=1}^{N} Q_{i,j} \cdot h_i^N(X_{\alpha}^{N-1}) \cdot h_j^N(X_{\beta}^{N-1}), \quad \alpha, \beta = 1, 2, \dots, N-1,$$
(27)

where Q and \hat{Q} represent solutions of N-th and (N-1)-th order respectively, and the superscripts of the Lagrange bases and the SPs indicate N-th order. Note that Q is not in a bold style since only one component of the vector of the conserved variables is used. Then the solutions are reconstructed in the level of (N-1)-th order and interpolated back to the level of N-th order, i.e.,

$$\bar{Q}_{i,j} = \sum_{\beta=1}^{N-1} \sum_{\alpha=1}^{N-1} \hat{Q}_{\alpha,\beta} \cdot h_{\alpha}^{N-1}(X_i^N) \cdot h_{\beta}^{N-1}(X_j^N), \quad i, j = 1, 2, \dots, N,$$
(28)

which is called prolongation. Here, \bar{Q} represents the solution which has been smoothed. Following [31], the smoothness sensor within each element is defined as

$$s_e = \log_{10} \left[\frac{(Q - \bar{Q}, Q - \bar{Q})_e}{(Q, Q)_e} \right],$$
 (29)

where $(\cdot, \cdot)_e$ is the standard inner product in the element. To prevent the denominator from being zero, $(Q, Q)_e$ is computed as $(Q + \epsilon, Q + \epsilon)_e$ in practical computation, where ϵ is a small number, which equals to 10^{-7} in the current study. Then the artificial dissipation term is evaluated as

$$f_{\Delta}(Q) = \begin{cases} 0 & \text{for } s_e < s_0 - \kappa, \\ \frac{f_0}{2} \left[1 + \sin \frac{\pi(s_e - s_0)}{2\kappa} \right] & \text{for } s_0 - \kappa \le s_e \le s_0 + \kappa, \\ f_0 & \text{for } s_e > s_0 + \kappa, \end{cases}$$
(30)

where f_0 , s_0 and κ are empirical parameters, which should be chosen for specific problems. In this study, the artificial viscosity and resistivity are computed as

$$\mu_{\Delta} = f_{\Delta}(\rho), \quad \eta_{\Delta} = (f_{\Delta}(B_x) + f_{\Delta}(B_y) + f_{\Delta}(B_z))/3. \tag{31}$$

To provide appropriate dissipation, following the suggestion in [33], f_0 is computed from the maximum absolute value of the characteristic speed and the element size h as

$$\mu_0 = C_\mu \lambda_{\text{max}} h / (N - 1),$$

$$\eta_0 = C_\eta \lambda_{\text{max}} h / (N - 1),$$
(32)

where μ_0 and η_0 are the value of f_0 for formulating μ_{Δ} and η_{Δ} respectively. Unless pointed out specifically, C_{μ} and C_{η} are chosen as 1. For simplicity, s_0 and κ are chosen as -3 and 3 respectively in all computational cases.

4. THE UNSTAGGERED CONSTRAINED TRANSPORT (CT) METHOD

The first three conservation laws in equation 1 form the Euler sub-system. The fourth conservation law in equation 1 governs the time evolution of the magnetic field and is called the induction equation. It can be rearranged into a form of cross product operator as

$$\partial_t \mathbf{B} = \nabla \times (\mathbf{U} \times \mathbf{B}). \tag{33}$$

Taking the divergence of equation 33, we have

$$\partial_t(\nabla \cdot \mathbf{B}) = \nabla \cdot (\nabla \times (\mathbf{U} \times \mathbf{B})) = \mathbf{0},\tag{34}$$

since the divergence of the curl of a vector is always zero. Equation 34 means that the magnetic field will be divergence-free if the initial magnetic field is divergence-free,

$$\nabla \cdot \mathbf{B} = 0. \tag{35}$$

However, in numerical computation, the discrete divergence of the magnetic field is not zero due to the spatial discretization error. Brackbill and Barnes [1] pointed out that an unphysical force proportional to $\nabla \cdot \mathbf{B}$ and parallel to \mathbf{U} is introduced into the Euler sub-system. If $\nabla \cdot \mathbf{B}$ cannot be controlled below a low value, this unphysical force can cause numerical instability and decrease the accuracy of the numerical computation.

In this paper, an unstaggered constrained transport (CT) framework proposed by Christlieb et al. [9] is used to satisfy the divergence-free condition in the discrete sense. Here a brief review of this framework is given. First, the divergence-free magnetic field **B** is written as the curl of the magnetic vector potential

$$\mathbf{B} = \nabla \times \mathbf{A}.\tag{36}$$

Plugging equation 36 into equation 33, we obtain

$$\nabla \times \left(\frac{\partial \mathbf{A}}{\partial t} + (\nabla \times \mathbf{A}) \times \mathbf{U} \right) = \mathbf{0}. \tag{37}$$

Using the Weyl gauge proposed in Helzel et al. [34], the governing equation of the magnetic vector potential becomes

$$\frac{\partial \mathbf{A}}{\partial t} + (\nabla \times \mathbf{A}) \times \mathbf{U} = \mathbf{0}. \tag{38}$$

For two-dimensional problems, it reduces to

$$\frac{\partial A_z}{\partial t} + u_x \frac{\partial A_z}{\partial x} + u_y \frac{\partial A_z}{\partial y} = 0.$$
 (39)

It is a hyperbolic partial differential equation. Therefore the spectral difference method can be a suitable method to solve it. The A_z at element interfaces is calculated as its upwind value.

The procedures to implement the unstaggered CT method is given then.

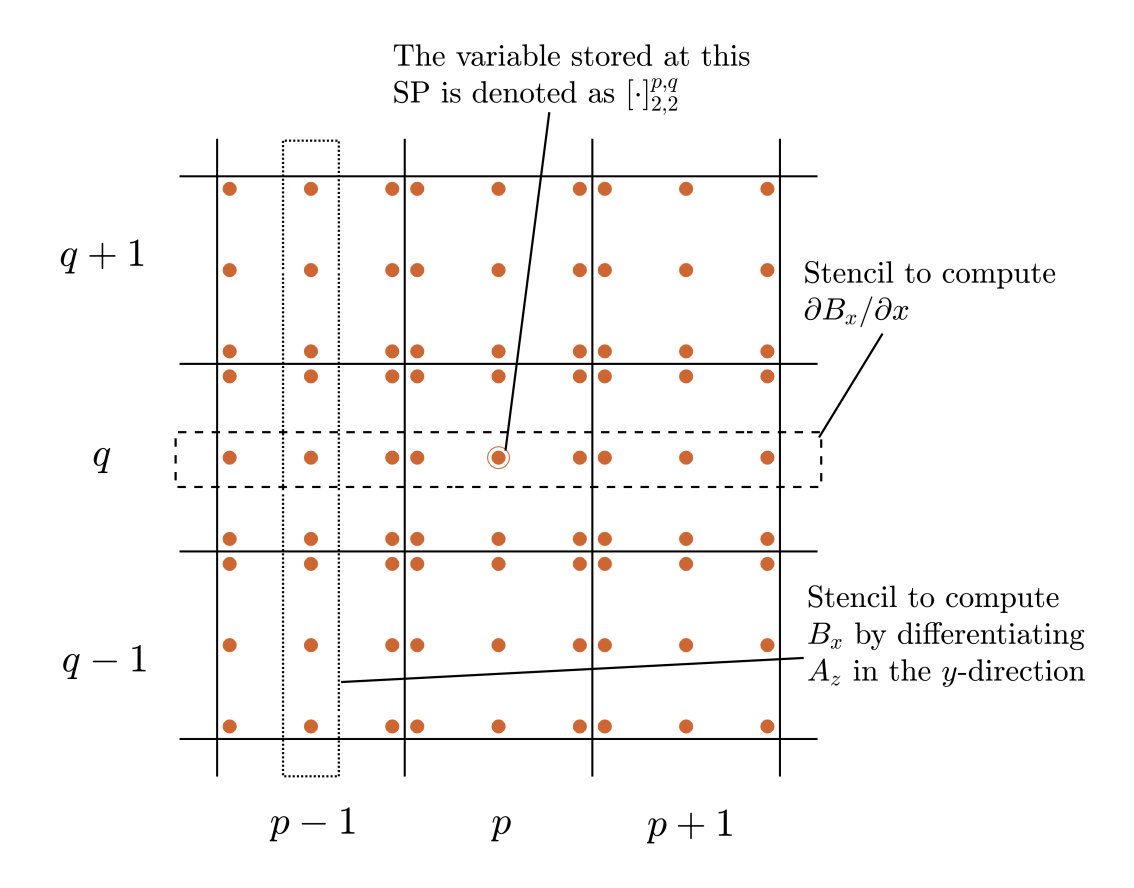


Figure 2: Illustration of the structured rectangular mesh and stencils used in the current SDCT method. $[\cdot]_{i,j}^{p,q}$ represents a variable stored at the (i,j)-th SP in the (p,q)-th element.

- Step 1: Start with the conserved variables and the magnetic potential at current time step: $\mathbf{Q}^n = (\rho^n, \rho \mathbf{U}^n, e^n, \mathbf{B}^n)^T$ and A_z^n .
- Step 2: Update the conserved variables $\mathbf{Q}^* = (\rho^{n+1}, \rho \mathbf{U}^{n+1}, e^{n+1}, \mathbf{B}^*)^T$ by solving equation 3 using the spectral difference method. Meanwhile, the magnetic potential A_z^{n+1} is updated independently by solving equation 39.
- Step 3: Use the procedures to compute gradients of solutions in the spectral difference method to evaluate the spatial derivatives of A_z and replace the predicted \mathbf{B}^* with the discrete curl of the magnetic potential A_z^{n+1} as

$$B_x^{n+1} = \frac{\partial A_z}{\partial y}, \quad B_y^{n+1} = -\frac{\partial A_z}{\partial x}.$$
 (40)

5. DISCRETE DIVERGENCE OF MAGNETIC FIELD

To implement Step 3 of the unstaggered CT method, equation 25 is employed to compute $\partial A_z/\partial y$ and $-\partial A_z/\partial x$ and subsequently use them to update the uncorrected magnetic field solved from the induction equation. The traditional SD method directly solves the ideal MHD equations without using any CT method to correct the magnetic field. The present method is named as the Spectral Difference method with Constrained Transport (SDCT) because of the above correction step. For the structured rectangular meshes, it can be proven that the SDCT method can ensure the divergence-free condition in a discrete sense.

Figure 2 illustrates the construction of computational stencil for updating B_x and B_y using $\partial A_z/\partial y$ and $-\partial A_z/\partial x$ as well as the indices used in the structured rectangular meshes. We use $[\cdot]_{i,j}^{p,q}$ to denote a variable stored at the (i,j)-th SP in the (p,q)-th element. According to the solution polynomials reconstructed in the interiors of each element and averaged solutions at the element interfaces described in equations 17 and 24, values of B_x at the FPs in the (p,q)-th

element are approximated as

$$[B_x]_{1/2,j}^{p,q} = 1/2 \cdot \left(\sum_{k=1}^{N} [B_x]_{k,j}^{p-1,q} h_k(X_{N+1/2}) + \sum_{k=1}^{N} [B_x]_{k,j}^{p,q} h_k(X_{1/2}) \right),$$

$$[B_x]_{N+1/2,j}^{p,q} = 1/2 \cdot \left(\sum_{k=1}^{N} [B_x]_{k,j}^{p,q} h_k(X_{N+1/2}) + \sum_{k=1}^{N} [B_x]_{k,j}^{p+1,q} h_k(X_{1/2}) \right),$$

$$[B_x]_{i+1/2,j}^{p,q} = \sum_{k=1}^{N} [B_x]_{k,j}^{p,q} h_k(X_{i+1/2}), \quad i = 1, 2, \dots, N-1.$$

$$(41)$$

Plugging these equations into equation 25, we obtain

$$\left[\frac{\partial B_x}{\partial x}\right]_{i,j}^{p,q} = \sum_{k=1}^{N} \mathbf{M}_{k,i}^{(-1)} [B_x]_{k,j}^{p-1,q} + \sum_{k=1}^{N} \mathbf{M}_{k,i}^{(0)} [B_x]_{k,j}^{p,q} + \sum_{k=1}^{N} \mathbf{M}_{k,i}^{(1)} [B_x]_{k,j}^{p+1,q},$$

$$= \sum_{r=p-1}^{p+1} \sum_{k=1}^{N} \mathbf{M}_{k,i}^{(r-p)} [B_x]_{k,j}^{r,q}.$$
(42)

where

$$\mathbf{M}_{\alpha,\beta}^{(-1)} = \frac{1}{2h_x} \cdot h_{\alpha}(X_{N+1/2}) \cdot l'_{1/2}(X_{\beta}),$$

$$\mathbf{M}_{\alpha,\beta}^{(0)} = \frac{1}{h_x} \cdot \sum_{k=1}^{N} h_{\alpha}(X_{k+1/2}) \cdot l'_{k+1/2}(X_{\beta}),$$

$$\mathbf{M}_{\alpha,\beta}^{(1)} = \frac{1}{2h_x} \cdot h_{\alpha}(X_{1/2}) \cdot l'_{N+1/2}(X_{\beta}) = \mathbf{M}_{N+\alpha-1,N+\beta-1}^{(-1)}.$$

$$\alpha = 1, 2, \dots, N, \quad \beta = 1, 2, \dots, N.$$

Note that $\mathbf{M}^{(-1)}$, $\mathbf{M}^{(0)}$ and $\mathbf{M}^{(1)}$ represent three different differentiation matrices. The superscript just serves as a sign to distinguish them and does not mean power of a matrix. Equation 42 is a mathematical expression of using the stencil in Figure 2 to compute $\partial B_x/\partial x$.

Note that the discrete values of B_x at all SPs are borrowed from the spatial derivative of the magnetic potential A_z with respect to y at the same locations. Therefore we have

$$[B_x]_{i,j}^{p,q} = \left(\frac{\partial A_z}{\partial y}\right)_{i,j}^{p,q} = \sum_{r=q-1}^{q+1} \sum_{k=1}^N \mathbf{M}_{k,j}^{(r-q)} [A_z]_{i,k}^{p,r},$$
(43)

as illustrated by the stencil to compute B_x in Figure 2. Combining equations (42) and (43), we obtain

$$\left[\frac{\partial B_x}{\partial x}\right]_{i,j}^{p,q} = \sum_{s=q-1}^{q+1} \sum_{r=p-1}^{p+1} \sum_{\beta=1}^{N} \sum_{\alpha=1}^{N} \mathbf{M}_{\alpha,i}^{(r-p)} \mathbf{M}_{\beta,j}^{(s-q)} [A_z]_{\alpha,\beta}^{r,s}.$$

$$(44)$$

To evaluate the discrete values of $\partial B_y/\partial y$, the same approach is used, and we obtain

$$\left[\frac{\partial B_y}{\partial y}\right]_{i,j}^{p,q} = \sum_{r=q-1}^{q+1} \sum_{k=1}^{N} \mathbf{M}_{k,j}^{(r-q)} [B_y]_{i,k}^{p,r}, \tag{45}$$

$$[B_y]_{i,j}^{p,q} = -\left(\frac{\partial A_z}{\partial x}\right)_{i,j}^{p,q} = -\sum_{r=p-1}^{p+1} \sum_{k=1}^N \mathbf{M}_{i,k}^{(r-p)} [A_z]_{k,j}^{r,q},\tag{46}$$

$$\left[\frac{\partial B_y}{\partial y}\right]_{i,j}^{p,q} = -\sum_{s=q-1}^{q+1} \sum_{r=p-1}^{p+1} \sum_{\beta=1}^{N} \sum_{\alpha=1}^{N} \mathbf{M}_{\alpha,i}^{(r-p)} \mathbf{M}_{\beta,j}^{(s-q)} [A_z]_{\alpha,\beta}^{r,s}.$$
 (47)

Summing equations (44) and (47), the divergence-free condition is satisfied at the SPs in the discrete sense:

$$\left[\frac{\partial B_x}{\partial x} + \frac{\partial B_y}{\partial y}\right]_{i,j}^{p,q} \equiv 0, \quad i, j = 1, 2, \cdots, N.$$
(48)

More generally, the spatial derivative of B_x along x direction at an arbitrary point ($\xi = \xi_0, \eta = \eta_0$) in the (p, q)-th element is computed as

$$\left[\frac{\partial B_x}{\partial x}\right]_{\xi=\xi_0,\eta=\eta_0}^{p,q} = \sum_{s=q-1}^{q+1} \sum_{r=p-1}^{p+1} \sum_{\beta=1}^{N} \sum_{\alpha=1}^{N} \mathbb{M}_{\alpha}^{(r-p)}(\xi_0) \cdot \mathbb{M}_{\beta}^{(s-q)}(\eta_0) \cdot [A_z]_{\alpha,\beta}^{r,s}$$
(49)

while the $\partial B_y/\partial y$ at the same location takes an exactly opposite expression, where the differentiation matrix M take the value

$$\mathbb{M}_{\alpha}^{(-1)}(\zeta) = \frac{1}{2h_x} \cdot h_{\alpha}(X_{N+1/2}) \cdot l'(\zeta), \tag{50}$$

$$\mathbb{M}_{\alpha}^{(0)}(\zeta) = \frac{1}{h_x} \cdot \sum_{k=1}^{N} h_{\alpha}(X_{k+1/2}) \cdot l'_{k+1/2}(\zeta), \tag{51}$$

$$\mathbb{M}_{\alpha}^{(1)}(\zeta) = \frac{1}{2h_r} \cdot h_{\alpha}(X_{1/2}) \cdot l'_{N+1/2}(\zeta). \tag{52}$$

Note that M is related to M as

$$\mathbf{M}_{\alpha,\beta}^{(k)} = \mathbb{M}_{\alpha}^{(k)}(X_{\beta}), \quad k = -1, 0, 1.$$
 (53)

So far, we have shown that the unstaggered CT method based on the spectral difference scheme preserves $\nabla \cdot \mathbf{B} = 0$ exactly by construction in a global and discrete sense.

6. THE 'SHIFTED' BOUNDARY CONDITION FOR THE MAGNETIC POTENTIAL

The Boundary Conditions (BCs) of compressible MHD simulations only set constraints to conserved variables $(\rho, \rho \mathbf{U}, e, \mathbf{B})^T$. But the magnetic potential A_z is a quantity which does not have explicit boundary conditions. In this section, a BC will be proposed for the magnetic potential A_z to ensure that the divergence-free constraint is satisfied even in elements abutting the boundaries.

Derivation in Section 5 shows that one underlying premise for the discrete $\nabla \cdot \mathbf{B} = 0$ in a specific element is that this element is located in the interior of the computational domain, or in other words, not immediately adjacent to the boundaries, since the derivation is based on an assumption that this element has eight neighboring elements in the cardinal and ordinal directions. If this element abuts a boundary which uses periodic BC for A_z , the periodic BC acts just like an element interface in the interior domain to connect two paired boundary faces, therefore, the discrete divergence-free property of the SDCT method is preserved even in these boundary elements. For example, four sides of the boundary of the Orzag-Tang vortex problem need periodic BCs for A_z . But in most other problems, even if boundaries give periodic BCs for conserved variables, the magnetic potential A_z is not always periodic. For example, in the rotor problem, the magnetic potential is initialized as $A_z(x,y) = B_{x,t_0}y$ in a square domain, A_z is discontinuous along the normal direction from the top to the bottom, even though all conserved variables are continuous along this direction.

To take care of this issue, we propose a 'shifted' periodic BC for magnetic potential A_z . These BCs are artificially imposed on boundaries which use periodic BCs for the conserved variables. They act just like the traditional periodic BC but solves the issue of discontinuity of A_z on paired boundary faces. For example, in the rotor problem, A_z is initialized as $B_{x,t_0}y_b$ on

the bottom boundary and $B_{x,t_0}y_t$ on the top boundary, where y_b and y_t are y-coordinate value of the bottom and top boundaries. The initial difference of A_z between the top and the bottom is $D_{A_z} = B_{x,t_0}(y_t - y_b)$. And this difference will be maintained until the end of the simulations. To compute gradients of A_z , the common A_z on the bottom and top faces are needed. After extrapolating A_z from solution points in the top and bottom boundary elements to the flux points on the bottom and top faces, the common A_z on these faces are computed by revising equation 24:

$$A_z^{\text{com,top}} = \frac{1}{2} (A_z^{\text{top}} + (A_z^{\text{bot}} + D_{A_z})),$$

$$A_z^{\text{com,bot}} = \frac{1}{2} ((A_z^{\text{top}} - D_{A_z}) + A_z^{\text{bot}}),$$
(54)

where A_z^{bot} and A_z^{top} refer to the extrapolation value of A_z on the bottom and top faces. To solve equation 39, the upwind magnetic potential A_z is needed on element interfaces. The bottom faces receive A_z from their paired top faces plus the initial difference while the top faces do the opposite.

7. NUMERICAL TESTS

7.1. 2D Discontinuous Magnetic Field Loop

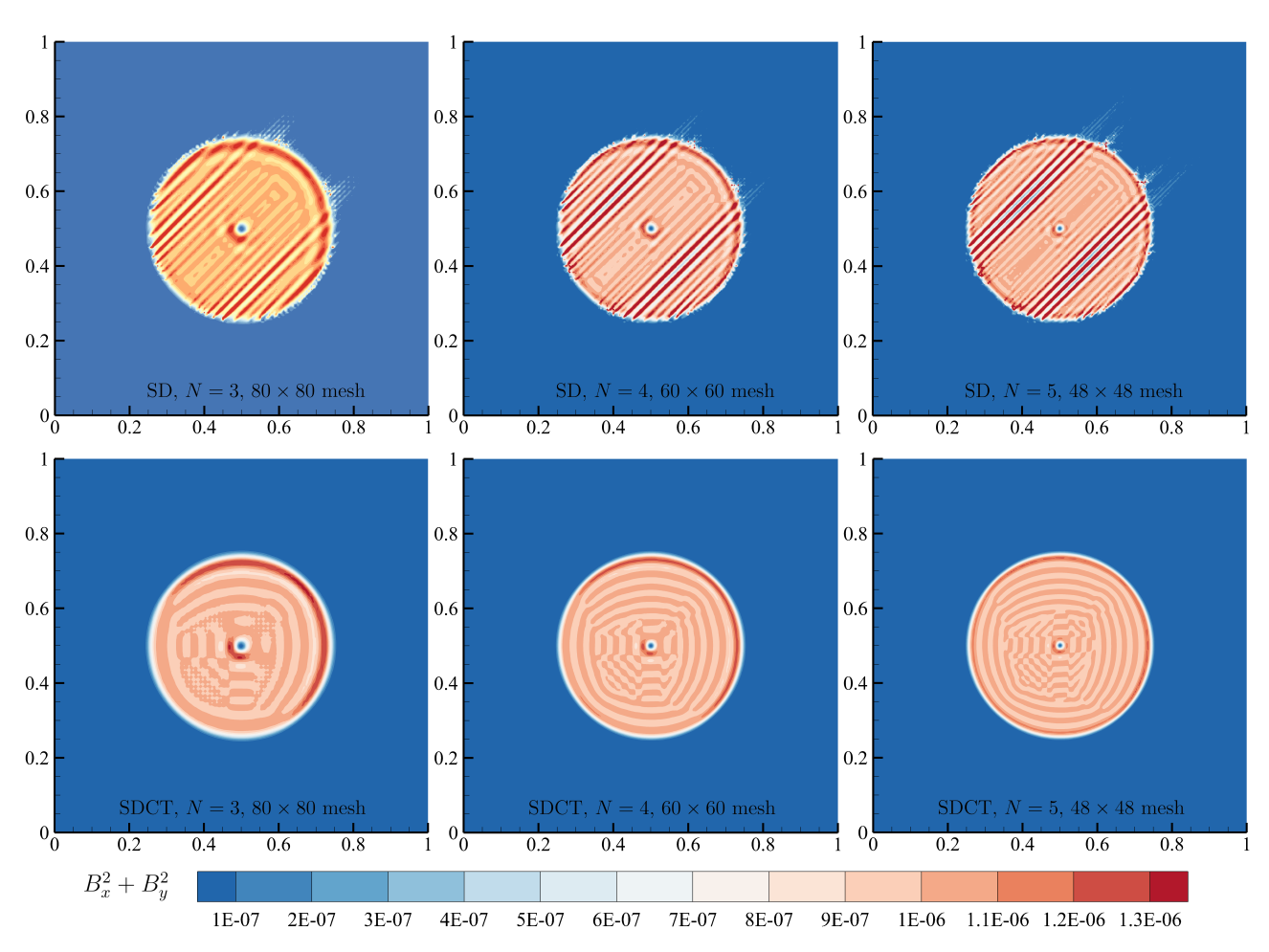


Figure 3: The magnetic pressure $B_x^2 + B_y^2$ of the magnetic field loop advection at t = 2.

The magnetic field loop problem is a well-known numerical experiment for the induction equation, i.e. equation 33. It was introduced in [35] to examine whether a MHD solver can maintain low divergence error and achieve magnetic energy conservation. It involves a weakly magnetized field loop advecting diagonally across the grid. The initial magnetic field is

$$(B_x, B_y) = (-A_0(y - y_c)/r, \quad A_0(x - x_c)/r) \quad \text{for} \quad r \le r_0,$$
 (55)

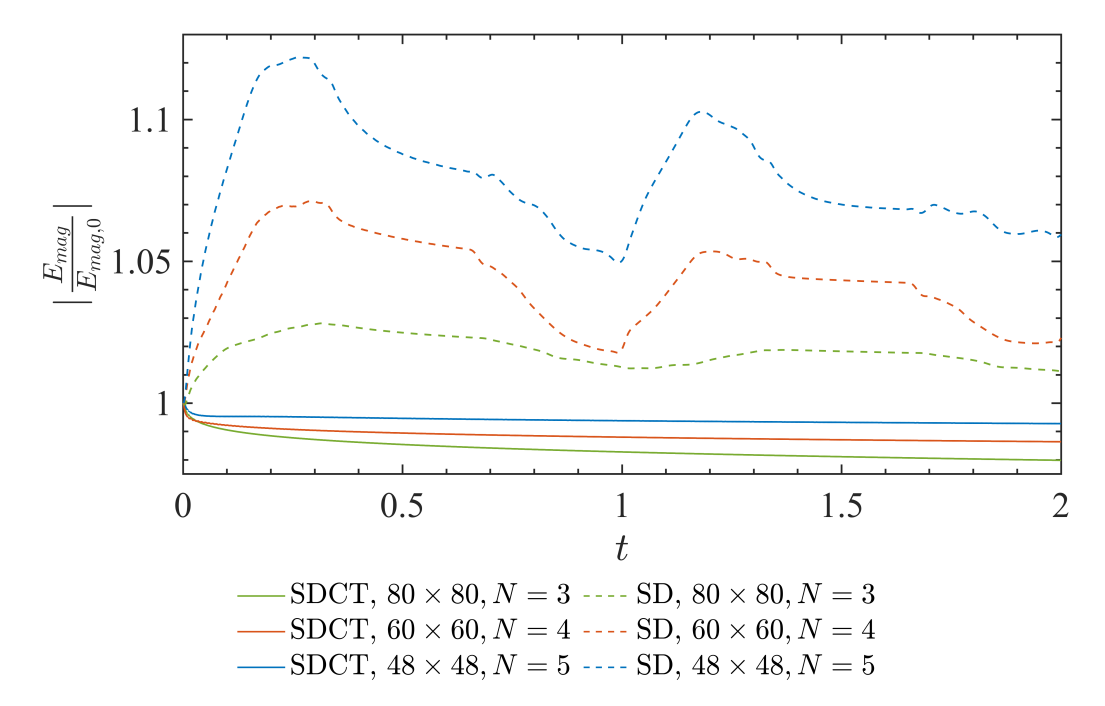


Figure 4: The time evolution of the magnetic energy of the magnetic field loop advection is shown to check whether the proposed SDCT method can avoid spurious magnetic dynamos induced by numerical errors.

and $\mathbf{B} = 0$ otherwise, and is advecting with a constant velocity field $\mathbf{U} = (1,1)$. Other constant parameters are $A_0 = 0.001, r_0 = 0.25, (x_c, y_c) = (0.5, 0.5)$. The computational domain is a square box $[0,1] \times [0,1]$. The total simulation time is t=2. Note that the time period to allow the loop to return to its original location is $\Delta T = 1$.

Three meshes $(80 \times 80 \text{ mesh with } N = 3, 60 \times 60 \text{ mesh with } N = 4 \text{ and } 48 \times 48 \text{ mesh}$ with N=5) are employed to carry out the simulation while maintaining the same number of degrees of freedom of the solutions. A comparison between results of the SDCT and SD method is performed. The SDCT method solves equation 39 and then predicts the magnetic field by computing the discrete curl of the magnetic potential A_z . On the other hand, the SD method directly solves equation 33 in its conservative form. Figure 3 shows that spurious stripes with high-frequency oscillations, aligned with the direction of the velocity field, appear when the standard SD method is used. By contrast, the SDCT method does not have this problem. When the polynomial degree N increases, the contour becomes more and more symmetrical and smooth, and the overshoot of the magnetic pressure decreases and approximates A_0^2 . In Figure 4, one can observe a spurious increase of the magnetic energy over time when the standard SD method is used, and interpret it wrongly as a dynamo. Moreover, the spurious dynamo induced by the numerical errors increases dramatically with the increase of the polynomial degree N. It implies that without proper treatment of the divergence error, increasing the polynomial degree cannot improve but degrade the accuracy of the numerical solution. By contrast, the spurious dynamo is not witnessed in the result of the SDCT method in Figure 4, and the numerical solution of the magnetic energy decays as expected owing to the numerical dissipation associated with the numerical method. With the increase of the polynomial degree N, the curve plotting the time evolution of the magnetic energy is more and more flat, which corresponds to the decrease of the numerical dissipation.

All the aforementioned properties achieved by the SDCT method are first found in a novel SD solver [21] for the induction equation (see their studies for a more in-depth discussion).

7.2. 2D Continuous Magnetic Field Loop

Following [21], in order to check whether the proposed method can achieve designed order of accuracy for solving the induction equation, the advection of a smooth and periodic magnetic field is considered. The initial magnetic field is

$$\mathbf{B} = (\cos(2\pi y), -\cos(2\pi x), 0). \tag{56}$$

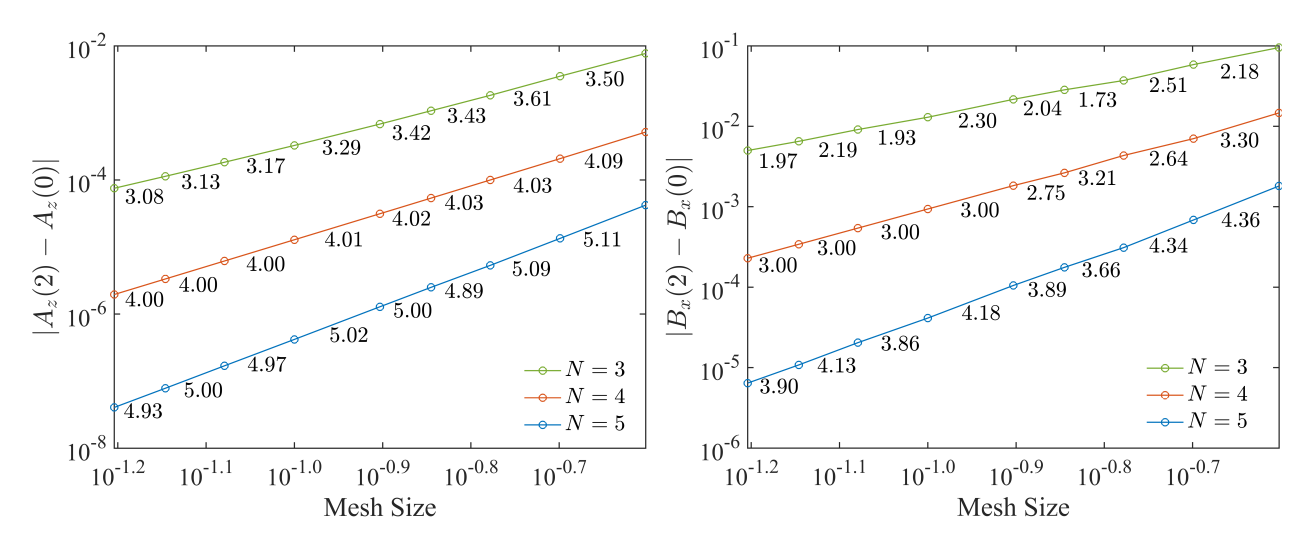


Figure 5: The convergence of the L^1 -error of A_z and B_x in the simulation of advection of the continuous magnetic field loop.

The velocity field is U = (1, 1). The computational domain is $[0, 1] \times [0, 1]$. The problem is computed to time t = 2 when the magnetic field will return back to its initial condition.

The solutions are computed on a series of $K \times K$ mesh, where K = 4, 5, 6, 7, 8, 10, 12, 14, 16. The L^1 -norm of the A_z and B_x error at t = 2 is plotted against the mesh size in the logarithmic scale in Figure 5. The subsequent orders of accuracy \mathcal{P} achieved are measured by comparing the error of two adjacent meshes in the sequence and are shown between two adjacent dots in Figure 5. They are computed by

$$\mathcal{P}_{L^p} = \frac{\log\left[\frac{\|\epsilon\|_p(\Omega^d)}{\|\epsilon\|_p(\Omega^{d+1})}\right]}{\log\left[\frac{\Delta(\Omega^d)}{\Delta(\Omega^{d+1})}\right]},\tag{57}$$

where p=1 to represent the norm, $\Delta(\Omega^i)=1/\sqrt{N_e}$, in which Ω^i denotes the computational domain meshed by the i-th grid in the sequence and N_e is the total number of elements. For the \mathcal{P} measured in terms of A_z , superconvergence is witnessed for the third-order SDCT method since all estimated orders of accuracy is higher than 3, especially when the meshes are sparse. For the fourth- and fifth-order SDCT methods, the desired orders of accuracy are achieved. For the \mathcal{P} measured in terms of B_x , the achieved orders of accuracy are approximately equal to N-1 for the N-th order SDCT method. The one-order reduction of accuracy for the magnetic field predicted by the SDCT method is induced during the process of performing the numerical curl of the magnetic potential to obtain the magnetic field. Similar reduction in the orders of accuracy are also presented in other CT methods in which the induction equation is solved by computing the evolution of the vector potential A [3, 5]. One way to avoid the reduction of accuracy is to design an independent set of 'staggered' stencil to compute the numerical curl of the magnetic potential. Under this new stencil, the order of accuracy in spatial discretization for the magnetic potential is typically one-order higher than what are used for the flow field. For example, Fu and Tang [10] used a fourth-order central difference scheme to discretize the curl operator of the magnetic potential to ensure that the order of accuracy of the MHD solver can reach up to eight. Nevertheless, for the present SDCT method, in order to keep the compactness of the stencil, the curl operator is just discretized using the same set of stencil as that for the flow field. Thus the SDCT method considered in this paper is an 'unstaggered method'.

Figure 5 shows that the subsequent order of accuracy estimated in terms of B_x is sometimes lower than that of the expected value. One factor that might trigger this is that Ω^{i+1} is not a nested refinement of Ω^i . If we only focus on the errors estimated on three nested meshes generated by successive refinement, as shown in Table 1, the estimated order of accuracy is completely consistent with our expected values.

Table 1: Errors and orders of accuracy of the simulation of advection of the continuous magnetic field loop measured on three nested meshes generated by successive refinement.

N_e	L^1 -error (A_z)	order (A_z)	L^1 -error (B_x)	order (B_x)
3rd order SDCT				
4×4	7.700E-3	-	9.519E-2	-
8×8	6.818E-4	3.50	2.162E-2	2.14
16×16	7.516E-5	3.18	4.997E-3	2.11
4th order SDCT				
4×4	5.179E-4	-	1.468E-2	-
8×8	3.136E-5	4.05	1.829E-3	3.00
16×16	1.957E-6	4.00	2.288E-4	3.00
5th order SDCT				
4×4	4.206E-5	-	1.810E-3	-
8×8	1.285E-6	5.03	1.050E-4	4.11
16×16	4.050E-8	4.99	6.418E-6	4.03

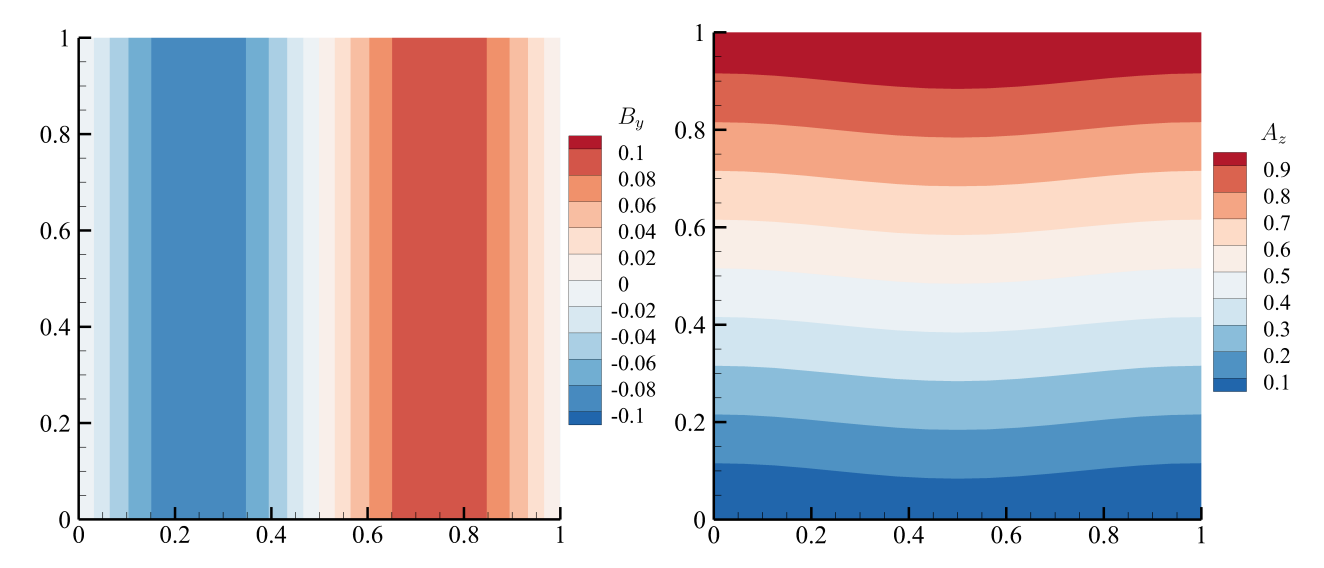


Figure 6: Contour plots of B_y and A_z of the propagation of the Alfvén wave at t = 0.5.

7.3. 2D Propagation of Alfvén Wave

The first MHD test problem is the propagation of a circularly polarized Alfvén wave [3]. It consists of a sinusoidal wave propagating at a constant speed in one dimension. The initial condition is

$$(\rho, u, v, w, p, B_x, B_y, B_z) = \frac{1}{10} (10, 0, \sin 2\pi x, \cos 2\pi x, 1, 10, \sin 2\pi x, \cos 2\pi x),$$
(58)

with $\gamma = 5/3$. The magnetic potential is initialized as

$$A_z = \frac{1}{20\pi} \cos 2\pi x + y. \tag{59}$$

The computational domain is $[0,1] \times [0,1]$, and periodic boundary conditions are used except that the 'shifted' boundary condition for A_z is imposed on the top and bottom boundaries. Simulation time is t=5. Note that the propagation speed of the Alfvén wave is $|B_x|/\sqrt{\rho}=1$, and the wave will return back to its initial state when t becomes an integer.

Figure 6 shows that the contours computed from the SDCT method are accurate and smooth. Table 2 shows an order of accuracy study performed by computing the L_1 and L_2 norm error of v and B_y at t=2. Although one order of accuracy is lost while using the CT

No. of elements	L_1 error	L_1 order	L_2 error	L_2 order
3rd order scheme				
4×4	5.9536E-3	-	6.7228E-3	-
8×8	3.4907E-4	4.09	4.0175E-4	4.06
16×16	2.6098E-5	3.74	3.4738E-5	3.53
5th order scheme				
4×4	2.3351E-5	-	2.8277E-5	-
8×8	4.8323E-7	5.59	6.2227E-7	5.51
$\phantom{00000000000000000000000000000000000$	1.5380E-8	4.97	1.9848E-8	4.97

(a) Measured by v

No. of elements	L_1 error	L_1 order	L_2 error	L_2 order
3rd order scheme				
4×4	5.6181E-3	-	7.3903E-3	-
8×8	5.3355e-4	3.40	5.8386E-4	3.66
16×16	5.9692E-5	3.16	6.8744E-5	3.08
5th order scheme				
4×4	4.2453E-5	-	4.9596E-5	-
8×8	6.4533E-7	6.04	7.4319E-7	6.06
$\phantom{00000000000000000000000000000000000$	1.8372E-8	5.13	2.5683E-8	4.85

(b) Measured by B_{ν}

Table 2: Errors and orders of accuracy of the simulation of the propagation of the Alfvén wave.

method to correct the magnetic field, accuracy will be restored in solving the Euler sub-system to some extent. The interplay between these two effects is quite complicated. Table 2 shows that the desired orders of accuracy are achieved for the third- and fifth-order SDCT methods. However, the achieved orders of accuracy for the second- and fourth-order SDCT methods do not live up to the expected orders.

7.4. 1D High Mach Number MHD Flow

To validate the artificial dissipation method for shock capturing, the high Mach number MHD flow proposed in [36] is considered. Its initial condition is

$$(\rho, u, v, w, p, B_x, B_y, B_z) = \begin{cases} (1, 0, 0, 0, 1000, 0, 1, 0), & \text{if } x < 0, \\ (0.125, 0, 0, 0, 0.1, 0, -1, 0), & \text{otherwise,} \end{cases}$$
(60)

with $\gamma = 2$. The computational domain is [-1, 1]. The final simulation time is t = 0.012. The third-order SD (SD3) method is used to compute solutions on three meshes with the number of elements $N_e = 500, 1000$ and 2000. The reference solution is borrowed from [10], which is computed from the fifth-order WENO (WENO5) scheme with $N_e = 2000$.

In this case, if C_{μ} and C_{η} equal to 1, excessive dissipation will amplify the spurious oscillations. Figure 7 shows the solutions under the setup $C_{\mu} = C_{\eta} = 0.3$. The shock profile at $x \approx 0.563$ converges to the WENO5 profile with the mesh refinement. The only imperfect is that the discontinuity of B_y at $x \approx 0.365$ cannot be captured as sharp as the WENO5 profile even when the mesh is refined to $N_e = 2000$. The underlying reason is that the artificial resistivity here is so large that the artificial dissipation added to the induction equation smooths the profile of the magnetic field, as shown in Figure 8. A parametric study of C_{η} is performed in Figure 9. It shows that lowering down the C_{η} without breaking the stability of the solution can improve the accuracy of the solution of the magnetic field near discontinuity significantly. By contrast, the solution of density already converges with the decrease of C_{η} . How to choose

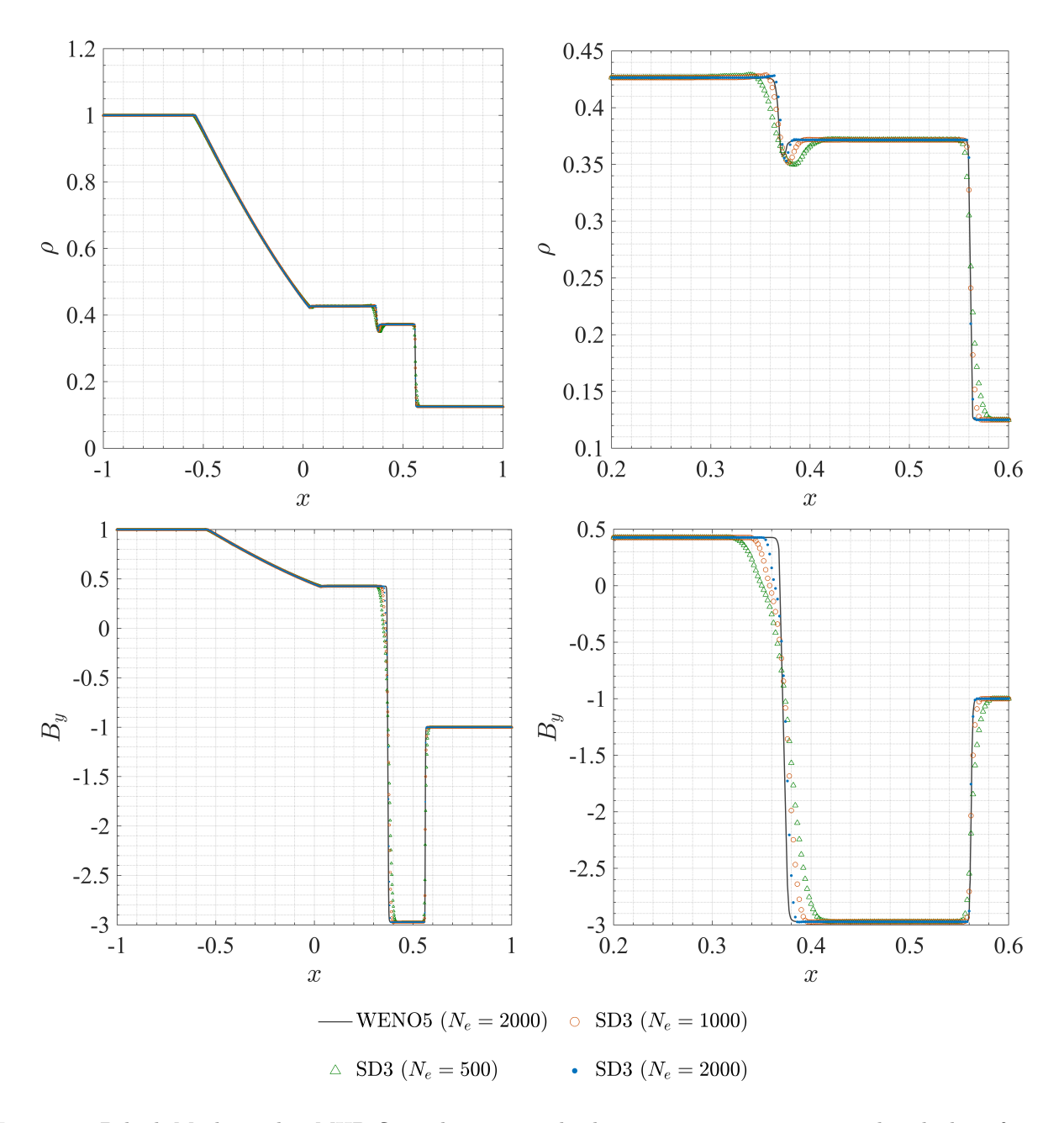


Figure 7: 1D high Mach number MHD flow: the computed solutions at t = 0.012 compared with the reference.

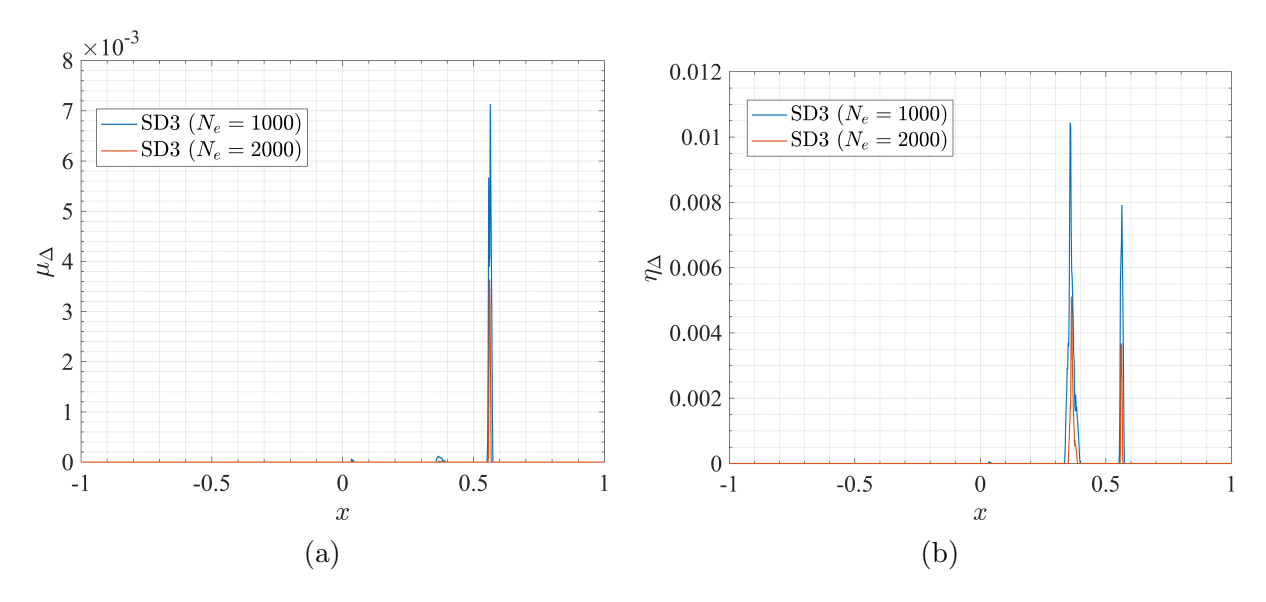


Figure 8: 1D high Mach number MHD flow: (a) artificial viscosity, (b) artificial resistivity at t = 0.012.

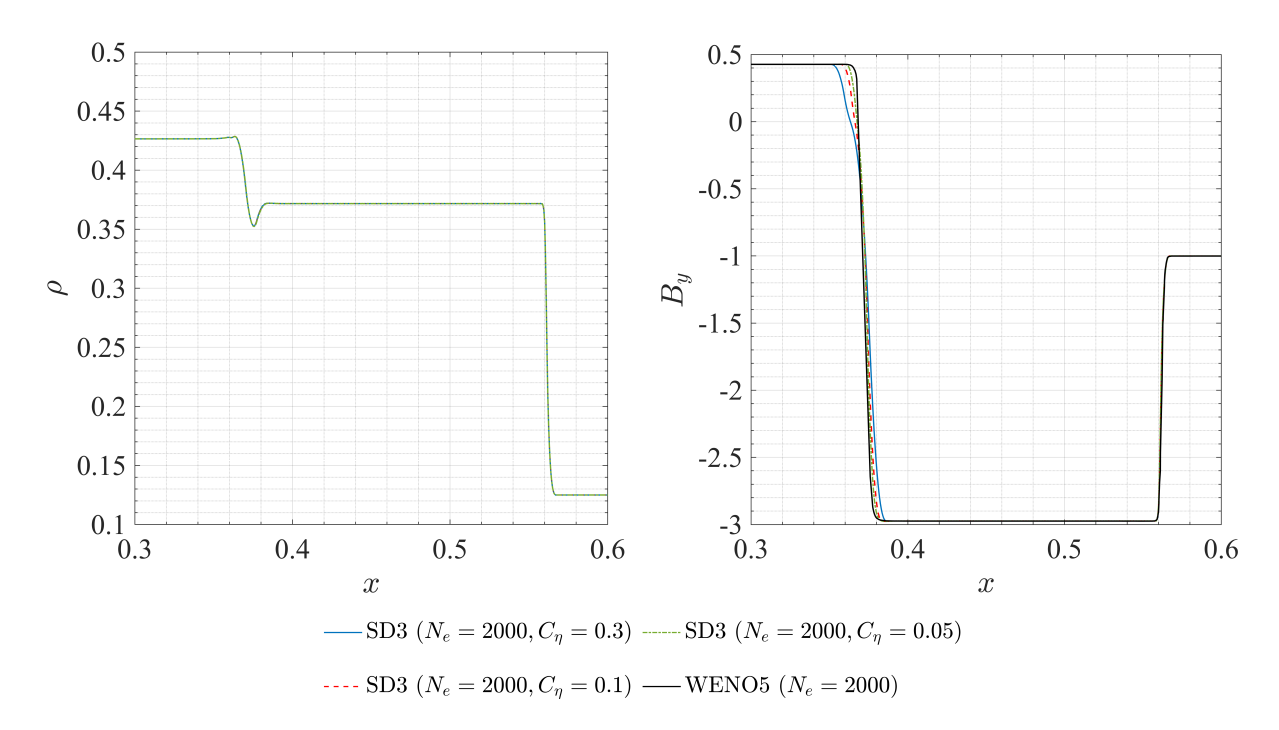


Figure 9: Computed solutions when C_{η} is chosen as 0.3, 0.1 and 0.05.

appropriate parameters for the artificial dissipation term without repeated manual adaptation is still an open question.

7.5. 1D MHD Shu-Osher Problem

For compressible fluid flow, the Shu-Osher problem introduced in [37] is a common benchmark to test the capability of high-order schemes to resolve small-scale flow structures in the presence of shocks. Susanto recently extended it to its MHD version in [38]. Its initial condition is

$$(\rho, u, v, w, p, B_x, B_y, B_z) = \begin{cases} (3.5, 5.8846, 1.1198, 0, 42.0267, 1, 3.6359, 0), & \text{if } x < -4, \\ (1 + 0.2\sin 5x, 0, 0, 0, 1, 1, 1, 0), & \text{otherwise,} \end{cases}$$
(61)

with $\gamma = 5/3$. The computation domain is [-5, 5]. The final simulation time is t = 0.7. The third-order SD (SD3) method is employed, and the mesh resolution is 500, 1000 and 2000. Results are compared with the reference solutions computed by the fifth-order WENO (WENO5) scheme on a mesh with $N_e = 2000$ documented in [10].

Figure 10 shows that all the computed solutions from the SD method are consistent with the reference. Even on a relatively sparse mesh $N_e = 500$, the phase difference of the solutions from the SD3 and the reference in the region of high-frequency entropy waves, $x \in (0.2, 1.6)$, is too small to see. This characterizes that the numerical dispersion error is minor. When the mesh is refined successively, the extrema of the entropy waves can be captured more and more accurately. Figure 11 shows that the artificial viscosity and resistivity only adds to the regions with shocks and discontinuities. And it can be noticed that refinement of the mesh lowers down the excessive dissipation significantly.

7.6. Comments on the Difference between 1D and 2D MHD Simulations

All the aforementioned test cases which include shocks are 1D. For 1D cases, satisfying the $\nabla \cdot \mathbf{B} = 0$ is automatic. For 2D cases when the constrained transport is turned on, the magnetic potential and the magnetic field need to be synchronized. When the artificial resistive terms are added to the induction equation near shocks, there should be a correspondingly additional term on the right hand side of equation 39. However, how to achieve this goal in a stable way is not yet found out. Moreover, how to formulate a divergence-free-preserving artificial magnetic

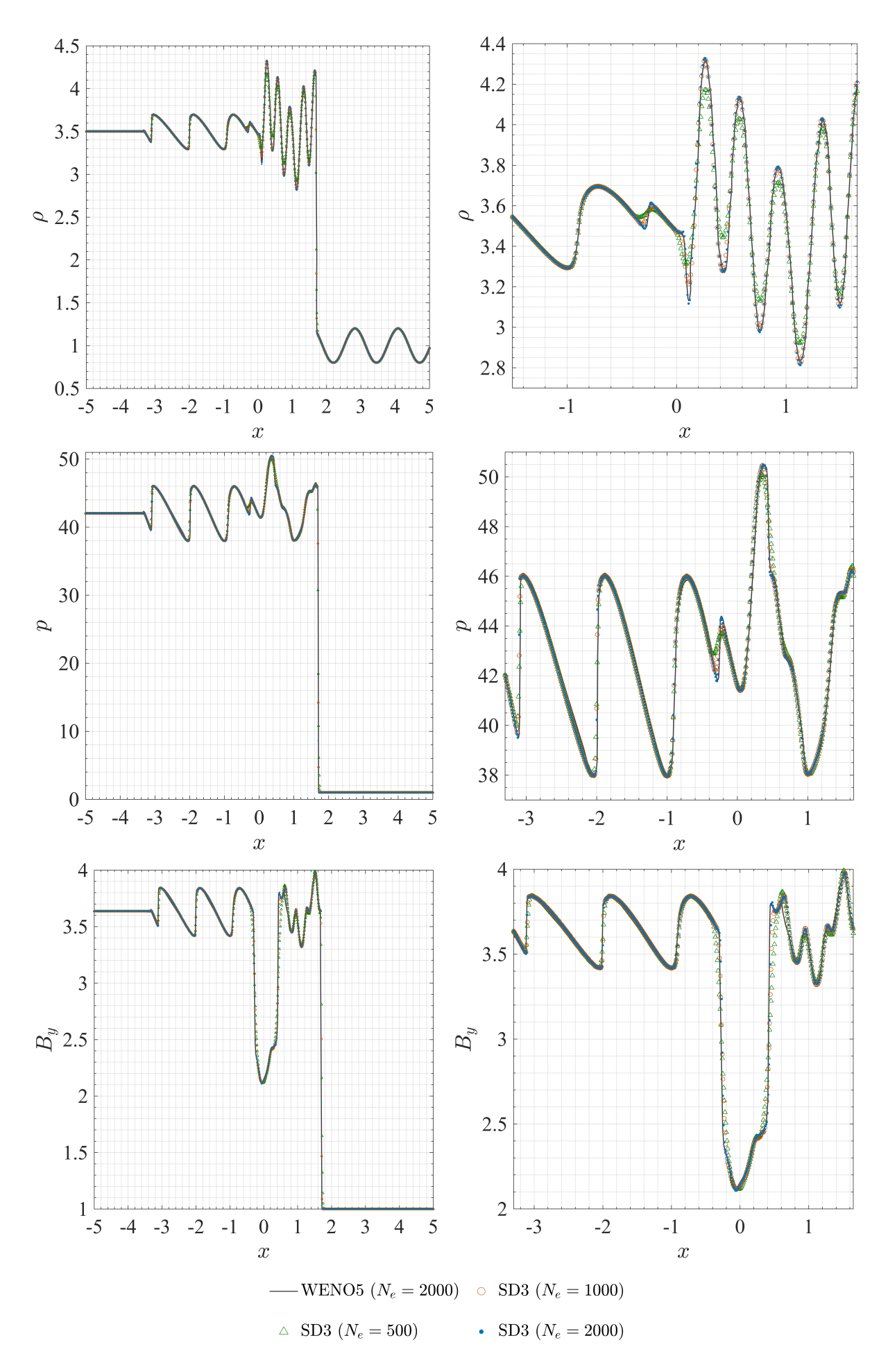


Figure 10: 1D MHD Shu-Osher problem: the computed solutions at t=0.7 compared with the reference.

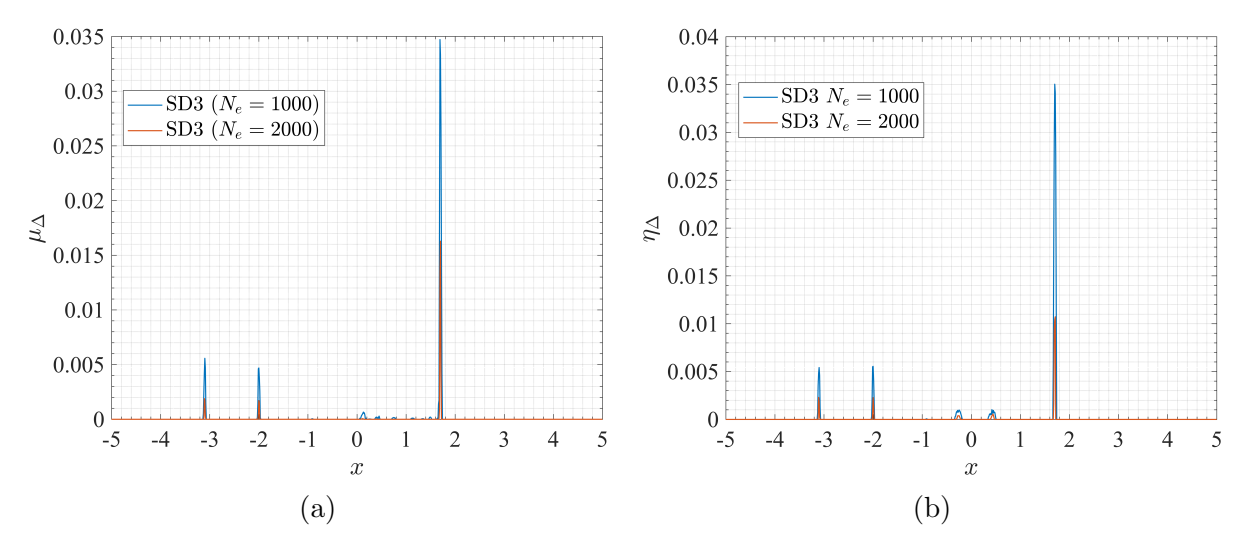


Figure 11: 1D MHD Shu-Osher problem: (a) artificial viscosity, (b) artificial resistivity at t = 0.7.

resistivity method, as discussed in [39], is not an easy task, especially when the divergence-free constraint should be maintained in the discrete sense. Fortunately, turning just the artificial viscosity on can resolve the spurious oscillations of most 2D cases with shocks.

7.7. 2D Orzag-Tang Vortex Problem

The Orzag-Tang vortex problem was first introduced in [40] as a model problem to study two-dimensional MHD turbulence. It is a challenging MHD problem as it involves complex shock interaction as the system evolves. The initial condition is

$$(\rho, u, v, w, p, B_x, B_y, B_z) = (\gamma^2, -\sin y, \sin x, 0, \gamma, -\sin y, \sin 2x, 0),$$
(62)

with $\gamma = 5/3$. The initial magnetic potential is

$$A_z(x,y) = 0.5\cos 2x + \cos y. \tag{63}$$

The computational domain is $[0, 2\pi] \times [0, 2\pi]$ with periodic boundary conditions.

To capture shocks sharply, the artificial viscosity is added in the non-smooth region. Since the artificial term is of an order of mesh size around shocks, the order of accuracy of the SD method will decrease to first order around shocks. Increasing the polynomial degree N cannot contribute significantly to high accuracy near discontinuities. Therefore a third order SDCT method is used in all 2D computations with shocks.

The predicted time development of density using the SDCT method is shown in Figure 12 until t=2. The solutions is completely smooth at t=0.5 and gradually develop discontinuous features then. Shocks emerging from four sides of the domain are clearly witnessed at t=1.5 and become strong at t=2. All these contours are in good agreement with the references [41, 42]. Figure 13 shows that the artificial viscosity is only added to narrow stripes of regions near the shocks and quickly diminishes in the smooth region. This ensures sharp shock capturing and preserves high accuracy of the solutions in the smooth region. The only issue that can be witnessed in the density contour at t=2 is that the solutions of the SDCT method is unphysical near (0,3.2) and $(2\pi,3.2)$. Weak instability appears here with unphysical discontinuity of the magnetic field. A potential explanation might be that lack of artificial magnetic resistivity leads to unphysical discontinuity. Since the artificial viscosity term only affects the Euler subsystem, there is not enough dissipation in the induction equation near the discontinuity of the magnetic field. Future works should include artificial magnetic resistivity or diffusion term in both the induction equation and the evolution equation of the magnetic potential A_z . Figure 14 shows that the divergence error is controlled at the order of magnitude of 10^{-11} , which nearly

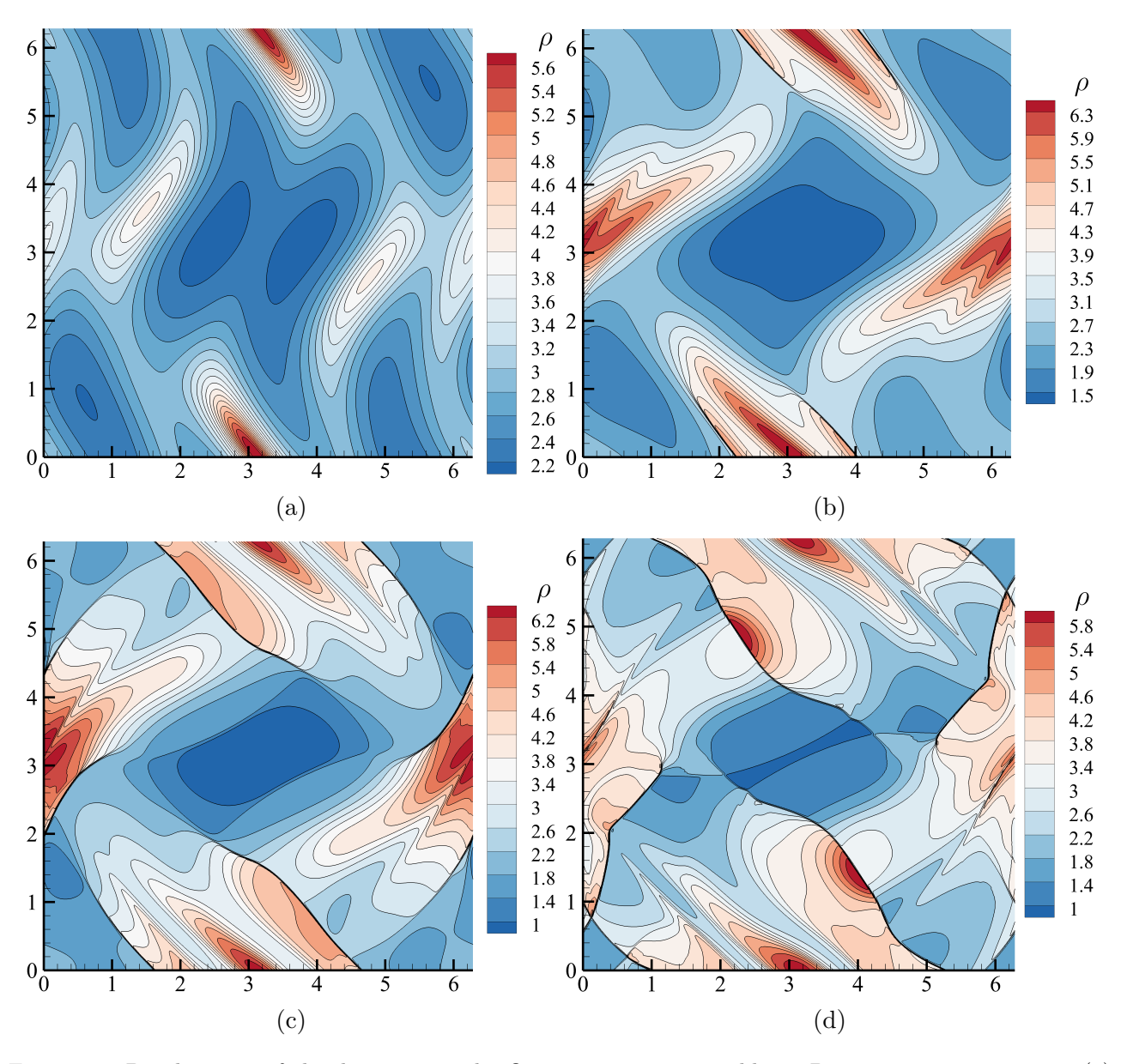


Figure 12: Development of the density ρ in the Orzag-Tang vortex problem. Density contours at times (a) t = 0.5, (b) t = 1, (c) t = 1.5 and (d) t = 2 are shown.

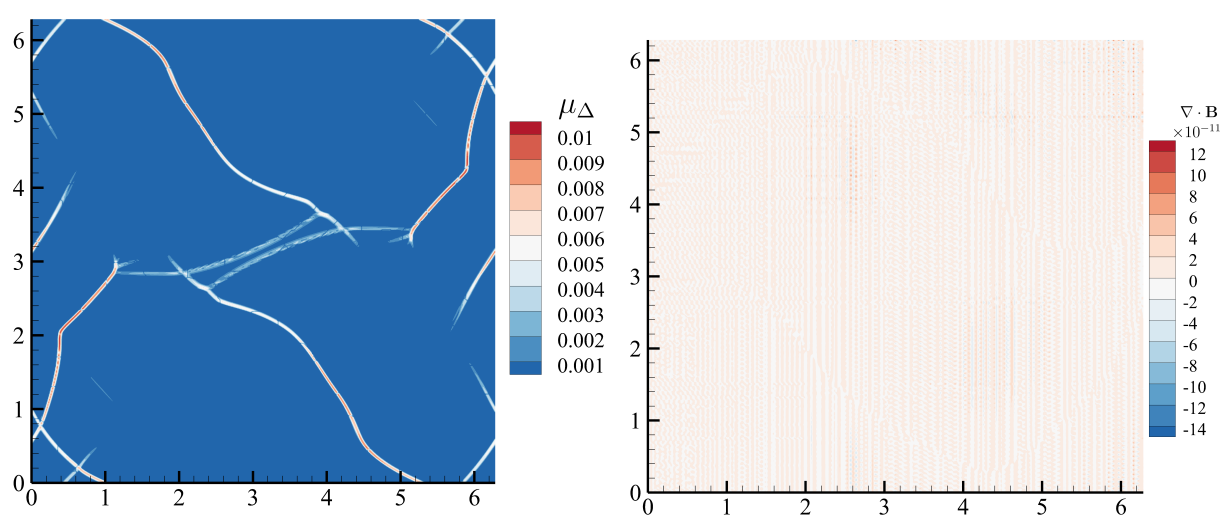


Figure 13: Plot of the artificial viscosity in the Orzag-Tang vortex problem computed on a 600 \times 600 mesh at t=2.

Figure 14: Divergence error contour of the magnetic field for the Orzag-Tang vortex problem at t=2.

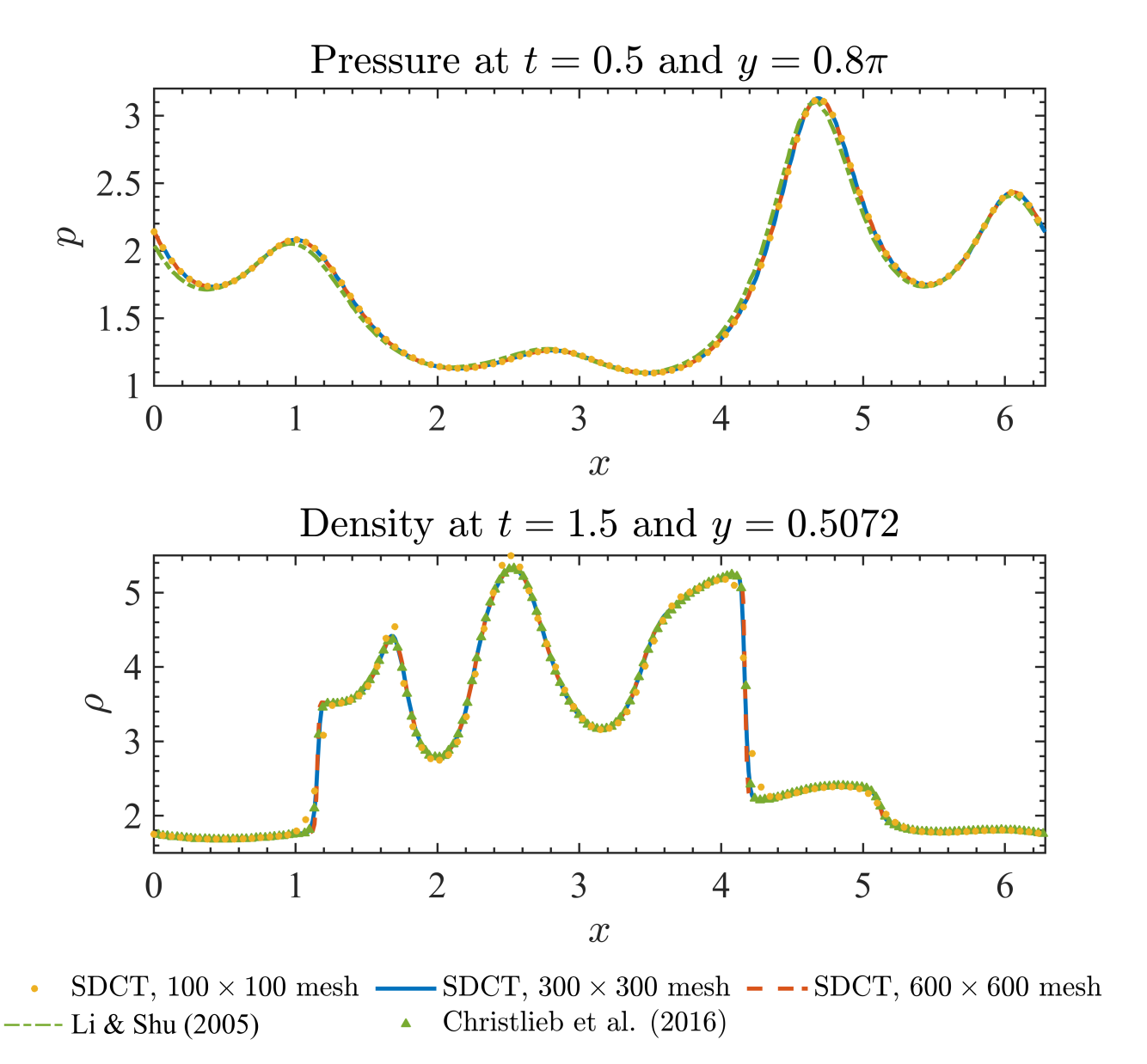


Figure 15: Orzag-Tang vortex problem. Comparison of the predicted pressure and density distribution of the SDCT method, the locally divergence-free discontinuous Galerkin method in the study of Li and Shu [41] and the finite difference weighted ENO method with unstaggered CT in the study of Christlieb et al. [42].

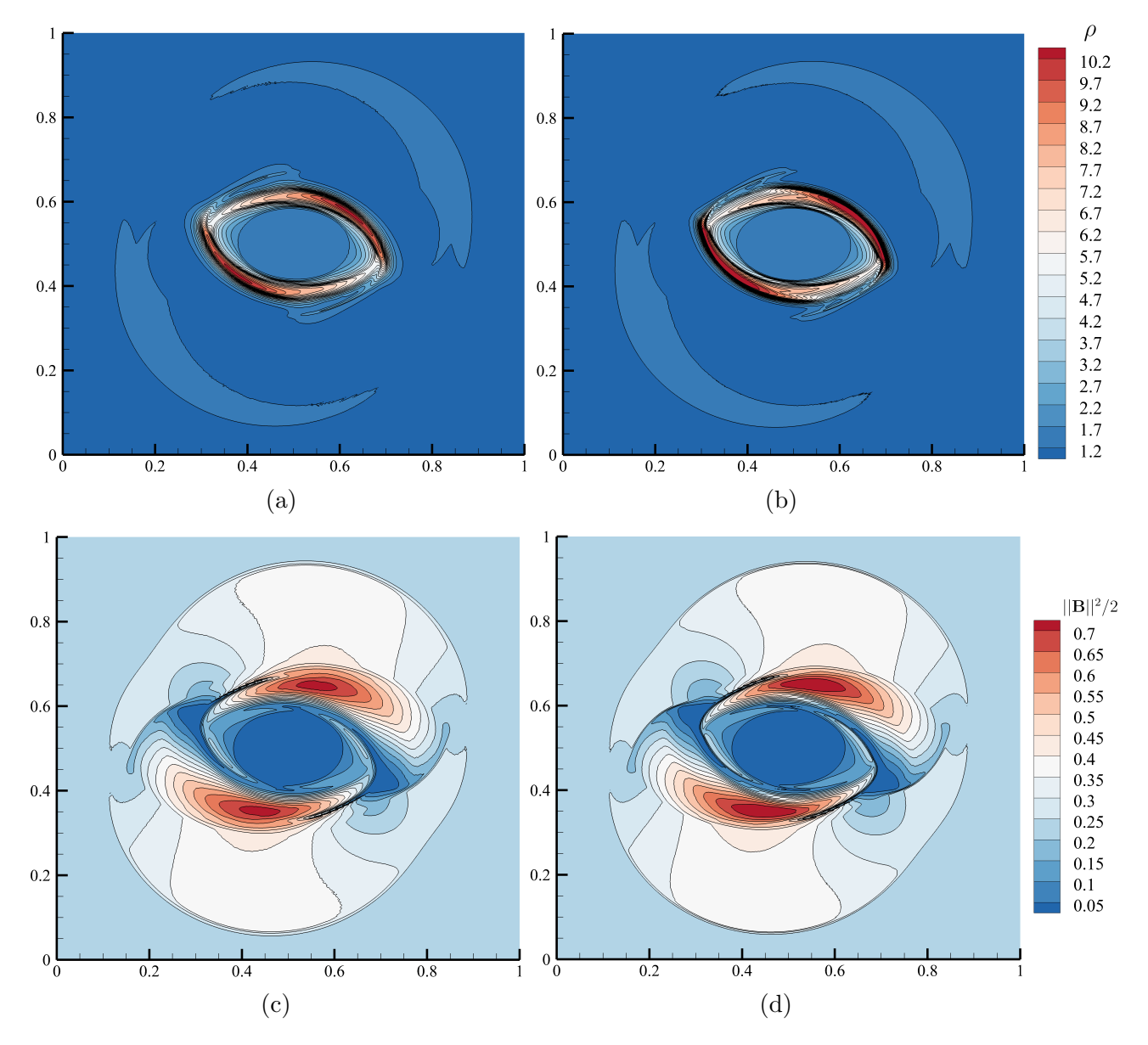


Figure 16: Density and magnetic pressure contours of the rotor problem at t = 0.27. (a) and (c): 400×400 mesh; (b) and (d): 800×800 mesh.

approach the machine precision. And it can be noticed that the distribution of the divergence error is arbitrary and not related to any MHD physics.

A mesh convergence study is performed by carrying out the computations on $100 \times 100, 300 \times 300$ and 600×600 meshes using the SDCT method. The cuts of pressure at t = 0.5 and $y = 0.8\pi$ and cuts of density at t = 1.5 and y = 0.5072 predicted on these three meshes are shown in Figure 15. It can be observed that the SDCT method can produce converged results even if discontinuities appear. And when the solutions are smooth, the SDCT method can obtain converged solutions on relatively sparse meshes. Moreover, to make a comparison with verified results, results of a locally divergence-free Discontinuous Galerkin (DG) method with total variation diminishing (TVD) limiter in the study of Li and Shu [41] and a finite difference weighted ENO (WENO) method with unstaggered CT in the study of Christlieb et al. [42] are also superimposed in Figure 15. The predicted pressure at t = 1.5 from the SDCT method agrees exactly with that from the WENO method with unstaggered CT. But small deviation is witnessed between the cuts of pressure predicted from the SDCT method and the DG method. One potential explanation is that the locally divergence-free bases cannot guarantee that $\nabla \cdot \mathbf{B}$ is exactly zero to the accuracy of machine round-off error.

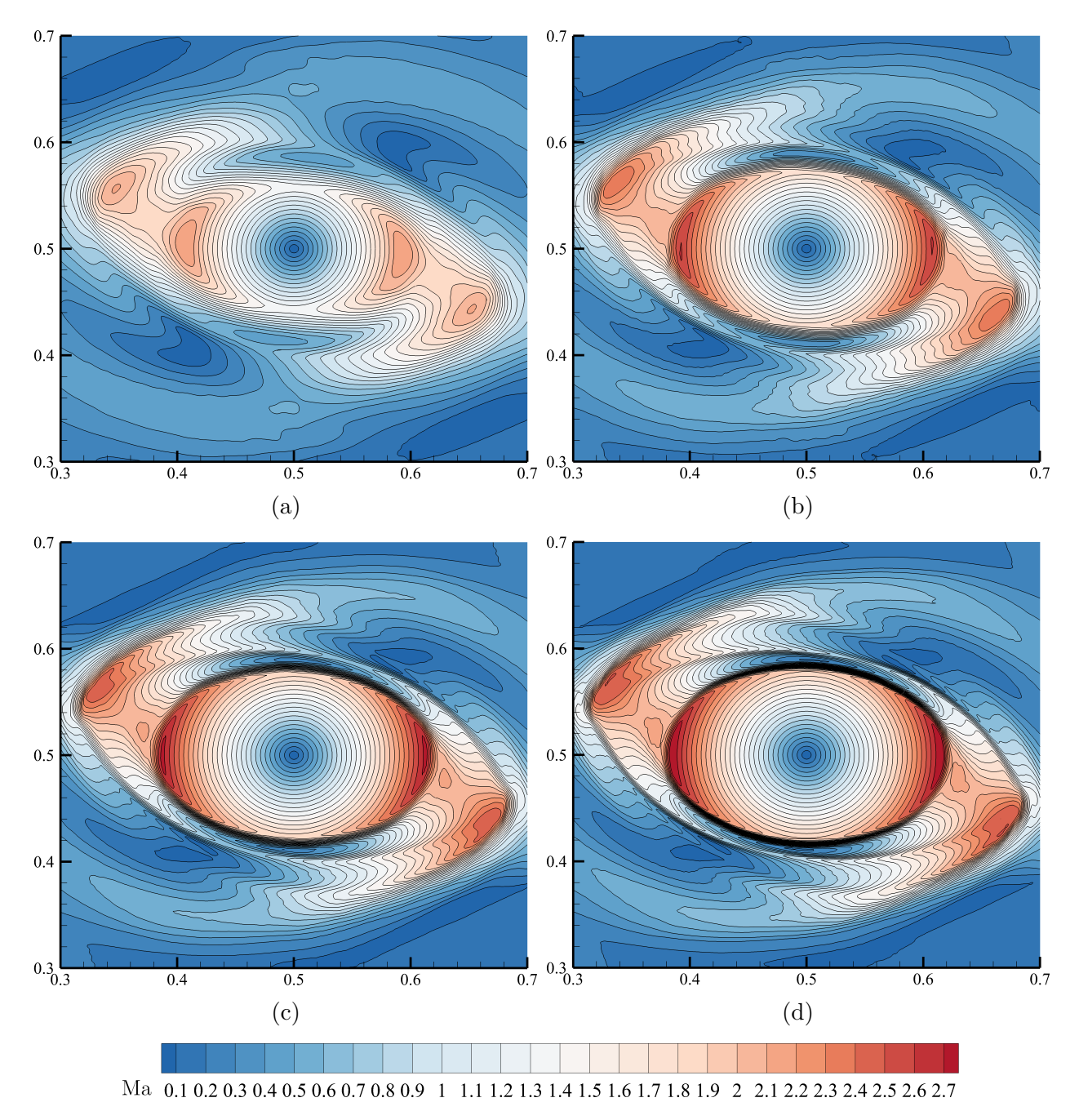


Figure 17: Zoom-in central part of the contours of Mach number at t = 0.27 in the rotor problem. (a): 200×200 mesh; (b): 400×400 mesh; (c): 600×600 mesh; (d): 800×800 mesh.

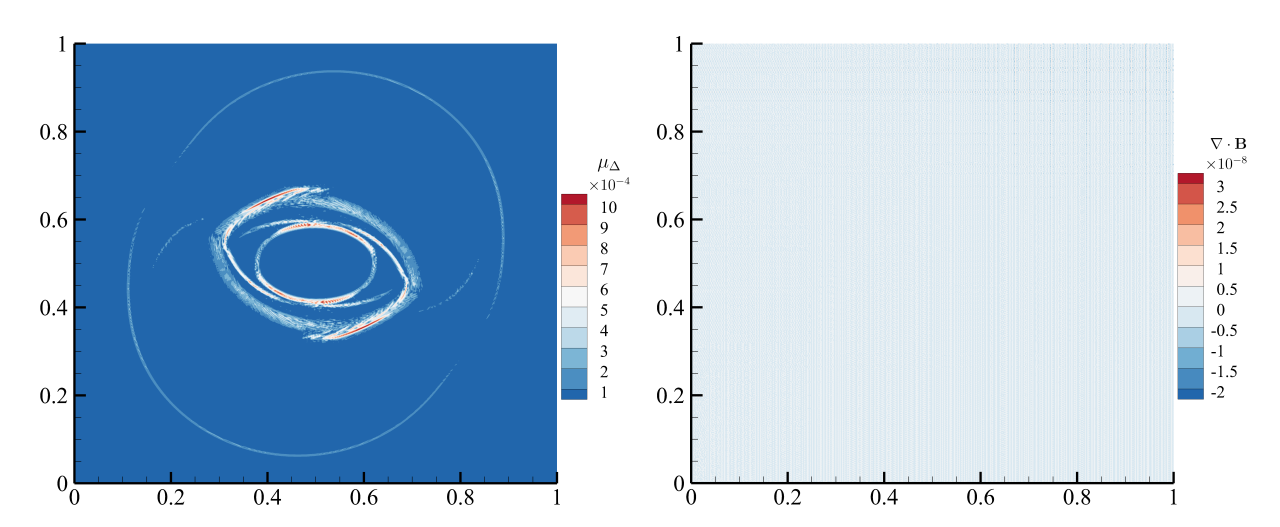


Figure 18: Plot of the artificial viscosity in the rotor Figure 19: Divergence error contour of the magnetic problem computed on a 800×800 mesh at t = 0.27. field for the rotor problem at t = 0.27.

7.8. 2D Rotor Problem

This two-dimensional test problem is first introduced in [2]. The problem describes a dense disk of fluid rotating rapidly while the light ambient fluid is still. The computation domain is $[0,1] \times [0,1]$, and periodic boundary conditions are used for four sides of the domain. The 'shifted' periodic boundary condition for magnetic potential A_z is used for top and bottom boundaries. The simulation time is $t \in [0,0.27]$. The initial setup follows that in [43, 42]:

$$\rho = \begin{cases}
10 & \text{if } r \leq r_0, \\
1 + 9\tilde{f}(r) & \text{if } r_0 < r < r_1, \\
1 & \text{if } r \geq r_1,
\end{cases} \quad u = \begin{cases}
-10y + 5 & \text{if } r \leq r_0, \\
(-10y + 5)\tilde{f}(r) & \text{if } r_0 < r < r_1, \\
0 & \text{if } r \geq r_1,
\end{cases}$$

$$v = \begin{cases}
10x + 5 & \text{if } r \leq r_0, \\
(10x - 5)\tilde{f}(r) & \text{if } r_0 < r < r_1, \\
0 & \text{if } r \geq r_1,
\end{cases} \quad w = 0,$$

$$0 & \text{if } r \geq r_1,$$

$$B_x = 2.5/\sqrt{4\pi}, \quad B_y = 0.0, \quad B_z = 0.0, \quad A_z = 2.5y/\sqrt{4\pi}, \quad p = 0.5,$$

$$r = \sqrt{(x - 0.5)^2 + (y - 0.5)^2}, \quad \tilde{f}(r) = \frac{1}{3}(23 - 200r),$$
(64)

where $r_0 = 0.1$ and $r_1 = 0.115$.

Many one step TVD base scheme fail for the rotor problem due to negative pressure [3]. However, in our simulations, no negative pressure is observed. The contour plots of density and magnetic pressure are shown in Figure 16. Computed results on mesh 400×400 and 800×800 match nearly exactly. The contours in the central part, which is featured by an oblate shape of rotating dense fluid, are quite smooth while some weak instabilities are observed outside the rotor. When the mesh is refined from 400×400 to 800×800 , the frequency of the instabilities becomes higher while the amplitude of that becomes smaller.

We also plot the Mach number for the central part while the mesh is refined in Figure 17 to check the convergence of the current SDCT method. The Mach number computed on the 200×200 mesh is underpredicted dramatically. This is mainly attributed to large numerical dissipation caused by low mesh resolution and more importantly, high artificial viscosity. With the refinement of the mesh, the Mach number contour gradually converges. Note that numerical solutions computed on the four meshes in Figure 17 do not show distortion, which is reported in [3,41]. [2,44] argue that such distortion is a consequence of the divergence error in the magnetic field. Therefore, no obvious sign of distortion might be attributed to the main advantage of the SDCT method, maintaining the divergence error under a low threshold.

Figure 18 shows that the artificial viscosity is only activated near discontinuities of the magnetic field, and the order of magnitude of it already decreases to 10^{-4} on a 800×800 mesh. Figure 19 shows that the divergence-free constraint is well preserved until t=0.27, and no sign of accumulation of divergence error is witnessed throughout the computation. Compared with the divergence error of the simulation of the Orzag-Tang vortex problem shown in Figure 14, the divergence error slightly increases to the order of magnitude of 10^{-8} . This is primarily caused by the fact that in practical computation, the initial difference of the magnetic potential A_z between top and bottom boundaries is calculated by using the extrapolated values instead of the exact values.

8. PARALLELIZATION AND COMPUTATIONAL COST

Parallelization of the current solver is to partition the computational domain and distribute the computational load among all processors in a balanced way. The METIS library [45] is employed to partition and distribute the mesh to all processors. Detailed description about how to conduct parallel computing based on the SD method is provided in [46]. Compared with using traditional SD method to solve the ideal MHD equation, in which 8 conserved variables

evolve in time, the SDCT method solves just one more equation about the magnetic potential. And the SDCT method has one additional procedure to compute the curl of the magnetic potential, which follows the way to compute gradients in the SD method. The computational cost of this procedure is also minor since in traditional SD method, calculation of gradients of 8 conserved variables are needed for computation of viscous fluxes. From this analysis, the extra computational cost of the SDCT method is less than 1/8 compared with the traditional SD method. Given that the artificial dissipation terms need to be calculated for cases with shocks, the ratio of extra computational cost is even lower in practical computation.

9. CONCLUSIONS

In this study, a two-dimensional high-order Spectral Difference algorithm with unstaggered Constrained Transport (SDCT) and a parallel computational code are successfully developed. To the best of our knowledge, this is the first solver that integrates the spectral difference scheme with the constrained transport method to solve the ideal MHD equations. It is shown that this solver can preserve the discrete divergence of the magnetic field to the accuracy of machine round-off error on structured rectangular meshes. Numerical benchmark tests demonstrate that due to its excellent property to maintain $\nabla \cdot \mathbf{B} = 0$, the SDCT method produces accurate simulation results. For MHD problems with smooth solutions, the SDCT method preserves the high-order accuracy of the SD method, although one-order of accuracy is sacrificed in the process of replacing the magnetic field with the curl of the magnetic potential. For problems with shocks, the SDCT method equipped with the artificial viscosity terms can capture shocks sharply and produce converged results through the mesh convergence study.

10. ACKNOWLEDGEMENT

The research work of both authors has been supported by a National Science Foundation (NSF) CAREER Award (No. 1952554) and an Air Force of Scientific Research (AFOSR) grant (Award No. FA9550-20-1-0374) monitored by Dr. Fariba Fahroo.

References

- [1] J. U. Brackbill, D. C. Barnes, The effect of nonzero $\nabla \cdot B$ on the numerical solution of the magnetohydrodynamic equations, Journal of Computational Physics 35 (1980) 426–430.
- [2] D. S. Balsara, D. S. Spicer, A staggered mesh algorithm using high order Godunov fluxes to ensure solenoidal magnetic fields in magnetohydrodynamic simulations, Journal of Computational Physics 149 (1999) 270–292.
- [3] G. Tóth, The $\nabla \cdot B = 0$ constraint in shock-capturing magnetohydrodynamics codes, Journal of Computational Physics 161 (2000) 605–652.
- [4] A. Dedner, F. Kemm, D. Kröner, C.-D. Munz, T. Schnitzer, M. Wesenberg, Hyperbolic divergence cleaning for the MHD equations, Journal of Computational Physics 175 (2002) 645–673.
- [5] C. R. Evans, J. F. Hawley, Simulation of magnetohydrodynamic flows-a constrained transport method, The Astrophysical Journal 332 (1988) 659–677.
- [6] P. Londrillo, L. Del Zanna, High-order upwind schemes for multidimensional magnetohydrodynamics, The Astrophysical Journal 530 (2000) 508.
- [7] D. S. Balsara, Divergence-free adaptive mesh refinement for magnetohydrodynamics, Journal of Computational Physics 174 (2001) 614–648.

- [8] J. A. Rossmanith, An unstaggered, high-resolution constrained transport method for magnetohydrodynamic flows, SIAM Journal on Scientific Computing 28 (2006) 1766–1797.
- [9] A. J. Christlieb, J. A. Rossmanith, Q. Tang, Finite difference weighted essentially non-oscillatory schemes with constrained transport for ideal magnetohydrodynamics, Journal of Computational Physics 268 (2014) 302–325.
- [10] L. Fu, Q. Tang, High-order low-dissipation targeted ENO schemes for ideal magnetohydrodynamics, Journal of Scientific Computing 80 (2019) 692–716.
- [11] D. A. Kopriva, K. J. H., A conservative staggered-grid Chebyshev multidomain method for compressible flows, Journal of Computational Physics 125 (1996) 244–261.
- [12] D. A. Kopriva, A staggered-grid multidomain spectral method for the compressible Navier-Stokes equations, Journal of Computational Physics 143 (1998) 125–158.
- [13] Y. Liu, M. Vinokur, Z. J. Wang, Spectral difference method for unstructured grids I: Basic formulation, Journal of Computational Physics 216 (2006) 780–801.
- [14] Z. J. Wang, Y. Liu, G. May, A. Jameson, Spectral difference method for unstructured grids II: extension to the Euler equations, Journal of Scientific Computing 32 (2007) 45–71.
- [15] B. J. Zimmerman, Z. J. Wang, M. R. Visbal, High-order spectral difference: verification and acceleration using GPU computing, in: 21st AIAA Computational Fluid Dynamics Conference, p. 2941.
- [16] J. Wang, C. Liang, M. S. Miesch, A compressible high-order unstructured spectral difference code for stratified convection in rotating spherical shells, Journal of Computational Physics 290 (2015) 90–111.
- [17] J. Wang, M. S. Miesch, C. Liang, Convection in oblate solar-type stars, The Astrophysical Journal 830 (2016) 45.
- [18] J. Yang, C. Liang, A high-order flux reconstruction adaptive mesh refinement method for magnetohydrodynamics on unstructured grids, International Journal for Numerical Methods in Fluids 86 (2018) 231–253.
- [19] X. Zhang, C. Liang, An open boundary condition for high-order solutions of magnetohydrodynamics on unstructured grids, International Journal of Computational Fluid Dynamics 34 (2020) 438–456.
- [20] X. Zhang, CHORUS-MHD Code for Solar and Planetary Magnetohydrodynamics, Ph.D. thesis, The George Washington University, 2019.
- [21] M. H. Veiga, D. A. Velasco-Romero, Q. Wenger, R. Teyssier, An arbitrary high-order spectral difference method for the induction equation, Journal of Computational Physics (2021) 110327.
- [22] H. T. Huynh, A flux reconstruction approach to high-order schemes including discontinuous Galerkin methods, in: 18th AIAA Computational Fluid Dynamics Conference, p. 4079.
- [23] C. Liang, A. Jameson, Z. J. Wang, Spectral difference method for compressible flow on unstructured grids with mixed elements, Journal of Computational Physics 228 (2009) 2847–2858.
- [24] K. Van den Abeele, C. Lacor, Z. J. Wang, On the stability and accuracy of the spectral difference method, Journal of Scientific Computing 37 (2008) 162–188.

- [25] A. Jameson, A proof of the stability of the spectral difference method for all orders of accuracy, Journal of Scientific Computing 45 (2010) 348–358.
- [26] P. D. Lax, Weak solutions of nonlinear hyperbolic equations and their numerical computation, Communications on pure and applied mathematics 7 (1954) 159–193.
- [27] P. L. Roe, D. S. Balsara, Notes on the eigensystem of magnetohydrodynamics, SIAM Journal on Applied Mathematics 56 (1996) 57–67.
- [28] F. Bassi, S. Rebay, A high-order accurate discontinuous finite element method for the numerical solution of the compressible Navier-Stokes equations, Journal of computational physics 131 (1997) 267–279.
- [29] Y. Sun, Z. Wang, Y. Liu, High-order multidomain spectral difference method for the Navier-Stokes equations, Communications in Computational Physics 2 (2007) 310–333.
- [30] S. Ruuth, Global optimization of explicit strong-stability-preserving Runge-Kutta methods, Mathematics of Computation 75 (2006) 183–207.
- [31] P.-O. Persson, J. Peraire, Sub-cell shock capturing for discontinuous Galerkin methods, in: 44th AIAA Aerospace Sciences Meeting and Exhibit, p. 112.
- [32] G. Lodato, L. Vervisch, P. Clavin, Direct numerical simulation of shock wavy-wall interaction: analysis of cellular shock structures and flow patterns, Journal of Fluid Mechanics 789 (2016) 221.
- [33] G. E. Barter, D. L. Darmofal, Shock capturing with pde-based artificial viscosity for dgfem: Part i. formulation, Journal of Computational Physics 229 (2010) 1810–1827.
- [34] C. Helzel, J. A. Rossmanith, B. Taetz, An unstaggered constrained transport method for the 3D ideal magnetohydrodynamic equations, Journal of Computational Physics 230 (2011) 3803–3829.
- [35] T. A. Gardiner, J. M. Stone, An unsplit Godunov method for ideal MHD via constrained transport, Journal of Computational Physics 205 (2005) 509–539.
- [36] G.-S. Jiang, C.-c. Wu, A high-order WENO finite difference scheme for the equations of ideal magnetohydrodynamics, Journal of Computational Physics 150 (1999) 561–594.
- [37] C.-W. Shu, S. Osher, Efficient implementation of essentially non-oscillatory shock-capturing schemes ii, Journal of Computational Physics 83 (1989) 32–78.
- [38] A. Susanto, L. Ivan, H. De Sterck, C. P. Groth, High-order central ENO finite-volume scheme for ideal MHD, Journal of Computational Physics 250 (2013) 141–164.
- [39] S. Kawai, Divergence-free-preserving high-order schemes for magnetohydrodynamics: an artificial magnetic resistivity method, Journal of Computational Physics 251 (2013) 292–318.
- [40] S. A. Orszag, C.-M. Tang, Small-scale structure of two-dimensional magnetohydrodynamic turbulence, Journal of Fluid Mechanics 90 (1979) 129–143.
- [41] F. Li, C.-W. Shu, Locally divergence-free discontinuous Galerkin methods for MHD equations, Journal of Scientific Computing 22 (2005) 413–442.
- [42] A. J. Christlieb, X. Feng, D. C. Seal, Q. Tang, A high-order positivity-preserving single-stage single-step method for the ideal magnetohydrodynamic equations, Journal of Computational Physics 316 (2016) 218–242.

- [43] K. Waagan, A positive MUSCL-Hancock scheme for ideal magnetohydrodynamics, Journal of Computational Physics 228 (2009) 8609–8626.
- [44] F. Li, L. Xu, S. Yakovlev, Central discontinuous galerkin methods for ideal MHD equations with the exactly divergence-free magnetic field, Journal of Computational Physics 230 (2011) 4828–4847.
- [45] G. Karypis, V. Kumar, A fast and high quality multilevel scheme for partitioning irregular graphs, SIAM Journal on scientific Computing 20 (1998) 359–392.
- [46] B. Zhang, C. Liang, J. Yang, Y. Rong, A 2D parallel high-order sliding and deforming spectral difference method, Computers & Fluids 139 (2016) 184–196.